SERI/TP-257-4366 • UC Category: 261 • DE91002190

Analysis of a Teetered, Variable-Speed Rotor

Final Report

Timothy L. Weber
Robert E. Wilson
Stel N. Walker
Department of Mechanical Engineering
Oregon State University
Corvallis, Oregon

SERI technical monitor: A. Wright

Solar Energy Research Institute
1617 Cole Boulevard
Golden, Colorado 80401-3393
A Division of Midwest Research Institute
Operated for the U.S. Department of Energy
under Contract No. DE-AC02-83CH10093

Prepared under Subcontract No. XG-0-19165-1

June 1991

NOTICE

Printed in the United States of America
Available from:
National Technical Information Service
U.S. Department of Commerce
5285 Port Royal Road
Springfield, VA 22161

Price: Microfiche A01
Printed Copy A04

Codes are used for pricing all publications. The code is determined by the number of pages in the publication. Information pertaining to the pricing codes can be found in the current issue of the following publications which are generally available in most libraries: *Energy Research Abstracts (ERA)*; *Government Reports Announcements* and Index (*GRA* and I); *Scientific and Technical Abstract Reports (STAR)*; and publication NTIS-PR-360 available from NTIS at the above address.

SUMMARY

A computer model of a horizontal axis wind turbine (HAWT) with four structural degrees of freedom has been derived and verified. The four degrees of freedom include flapwise motion of the blades, teeter motion, and variable rotor speed. Options for the variable rotor speed include synchronous, induction, and constant-tip speed generator models with either start, stop, or normal operations. Verification is made by comparison with analytical solutions and mean and cyclic ESI-80 data. The Veers full-field turbulence model is used as a wind input for a synchronous and induction generator test case during normal operation. As a result of the comparison, it is concluded that the computer model can be used to predict accurately mean and cyclic loads with a turbulent wind input.

TABLE OF CONTENTS

LIST OF FIGURES

NOMENCLATURE

$\mathbf{a}_i''$	-	inertial coordinate
$\mathbf{a}_i'$	-	yaw coordinate
$\mathbf{a}_i$	-	tilt and generator coordinate
$\mathbf{b}_i$	-	rotating rotor coordinate
$\mathbf{c}_i$	-	rotating teeter coordinate
$\mathbf{d}_i$	-	delta-3 coordinate
$\mathbf{e}_i$	-	precone coordinate
$\mathbf{f}_i$	-	elastic axis rotation c
$\mathbf{g}_i$	-	deflected blade coordinate
q_1	-	blade one deflection
q_2	-	blade two deflection
q_3	-	teeter angle
q_4	-	rotor angle
Q^{ij}	-	transformation from ith generator coordinate to jth blade coordinate
d	-	distance from tower centerline to teeter point
R_u	-	undersling length
u_{ij}	-	jth blade displacement in ith direction
r	-	distance to blade element
EI	-	blade stiffness
k	-	constant
b	-	constant
z	-	dimensionless blade radius
R	-	total blade length
R_H	-	hub length
w	-	weighting factor

$^{N}\mathbf{p}_{i}^{Q}$	-	position vector on ith blade of point Q in reference frame N
P_{ji}	-	magnitude of distance on ith blade in jth direction
$^{N}\mathbf{v}^{Q}$	-	velocity of point Q in reference frame N
Q	-	point on blade
N	-	generator reference frame
v_i	-	velocity magnitude in ith direction
w_i	-	angular velocity magnitude in ith direction
$^{N}\mathbf{a}^{Q}$	-	acceleration of point Q in reference frame N
$^{N}\mathbf{w}^{Q}$	-	angular velocity of point Q
a_i	-	acceleration magnitude in ith direction
T	-	rotor thrust
u_1	-	wake velocity
u	-	axial velocity component
v_∞	-	free-stream velocity
A	-	rotor area
L	-	lift
D	-	drag
ΔP	-	pressure differences across rotor
u_1	-	axial velocity component
a	-	axial induction factor
a_c	-	axial induction constant
C_T	-	thrust coefficient
C_P	-	power coefficient
F	-	Prandtl tip loss value
B	-	number of blades
C_L	-	lift coefficient
C_D	-	drag coefficient

c	-	chord length
W	-	relative air velocity
f_n, f_t	-	aerodynamic forces
F_r, F_r^*	-	generalized active and inertial forces
$\mathbf{v}_r^Q$	-	holonomic partial velocity
$\mathbf{R}$	-	resultant of external forces
$\mathbf{T}$	-	resultant of external torques
$\mathbf{I}$	-	inertia dyadic
u_r	-	generalized speed
N_{ri}	-	partial velocity magnitude in ith direction
R_i	-	resultant force magnitude in ith direction
g_r	-	generalized inertia term
$I_{generator}$	-	generator inertia
V	-	blade element potential energy
$F_{r_{HUB}}$, $F^*_{r_{HUB}}$	-	generalized active and inertial hub forces
M_{HUB}	-	hub mass
I_{HUB}	-	hub inertia
$T_{electrical}$	-	generator electrical restraining torque
T_{losses}	-	generator torque losses
C_e	-	constant
T_{fixed}	-	generator fixed loss
N	-	gearbox step-up ratio
$T_{variable}$	-	generator variable loss
P_{RATED}	-	generator rated power
f	-	generator fixed-loss factor
T_i	-	rotor torque at time step i
T_{GAIN}	-	torque gain

V_i	-	wind velocity at time step i
K_G	-	gain constant
V_{HUB}	-	hub velocity
H_{HUB}	-	hub height
n	-	wind shear exponent
y	-	distance from tower centerline
D	-	tower diameter
q_{static}	-	static tip deflection
w_n	-	natural frequency
g	-	gravity

Greek

$^N\alpha^Q$	-	angular accelreation of point Q
ω_r^Q	-	holonomic partial angular velocity
α	-	angle of attack
α_i	-	angular acceleration magnitude in ith direction
θ	-	blade twist
θ_p	-	elastic axis angle
β	-	precone
δ_3	-	delta-3
ζ	-	blade element rotation
ϕ_i	-	assumed mode shape in i direction
ϕ_a	-	mode shape for uniform loading
ϕ_b	-	mode shape for tip force
ρ	-	density
ϕ_α	-	induction angle
Ω	-	rotor angular velocity

Γ	-	tip-speed ratio
χ	-	tilt
μ	-	blade mass per unit length
η_{GB}	-	gearbox efficiency
Ω_o	-	rated rotor angular velocity
η_{Gen}	-	generator efficiency
Ω_R	-	nominal rotor angular velocity
λ	-	optimum tip-speed ratio
Ω_i	-	rotor speed at time step i
ϵ	-	tower shadow velocity deficit
π	-	pi

Mathematical

∂	-	partial
$(\dot{})$	-	time derivative

1. INTRODUCTION

The determination of inertial and aerodynamic loads is necessary for the design of horizontal axis wind turbines (HAWTs). Extensive work has been done predicting steady-state and cyclic blade and rotor loads [1-6] for constant speed HAWTs. Currently, variable-speed generators are being examined for use with HAWTs [7]. The effect of variable-speed operation on blade and rotor loads is not well known. Understanding variable-speed operation of HAWTs is critical because the rotor speed can coincide with many system natural frequencies. Instabilities and excitations near system natural frequencies can reduce working lifetimes of components and, in extreme cases, cause catastrophic failure. The wind turbine designer needs tools to predict potential trouble spots. This report develops techniques for analyzing the loads associated with variable speed operation of HAWTs.

The objective of this study was to develop a four-degree-of-freedom time-domain computer model of a two-bladed, teetered HAWT with a variable-speed rotor. The specific geometry was chosen to parallel projected development of HAWTs, that will have this configuration [8]. The computer code determines loads and response by combining a mathematical model having four degrees of freedom with aerodynamic loading. The aerodynamic loading consists of deterministic effects, such as wind shear, tower shadow, and yaw, with stochastic effects from wind turbulence.

1.1 Variable Speed

In order for variable speed to be economically viable, the additional cost of variable-speed equipment must be offset. These offsets are a combination of increased power capture from the wind and decreased loads, which result in longer turbine component lifetimes. In the past, this has not been the case; consequently, most HAWTs run at a fixed speed. Recently, the capital cost of the power transmission components used in variable-speed generators has decreased [7]. With this decrease, variable speed implementation has become a favorite candidate for use on the next generation of wind turbines. The advantages of variable-speed operation are numerous and have been extensively discussed, but the energy savings realized from using variable-speed systems are widely varied and often cannot be assigned a dollar value.

A typical HAWT rotor power coefficient (Cp) versus tip speed ratio (Γ) is shown in Figure 1.1. A fixed-speed wind turbine can be designed to have an optimum power coefficient at only one wind speed. When the wind speed is either higher or lower than this optimum wind speed, the aerodynamic efficiency is reduced. A variable-speed turbine can operate with a optimum power coefficient by varying the rotor speed proportionally to the wind speed. This results in increased power capture over fixed-speed operation. Predictions of increased power have been widely varied, from 3% to 6% [9] up to 10% to 20% [10].

A variable-speed machine can reduce the power and load fluctuations caused by rapid changes in the wind. When a fixed-speed machine experiences a gust or wind deficit, the machine experiences a change in torque, which consequently changes the power sent to the utility [11]. This has dis-

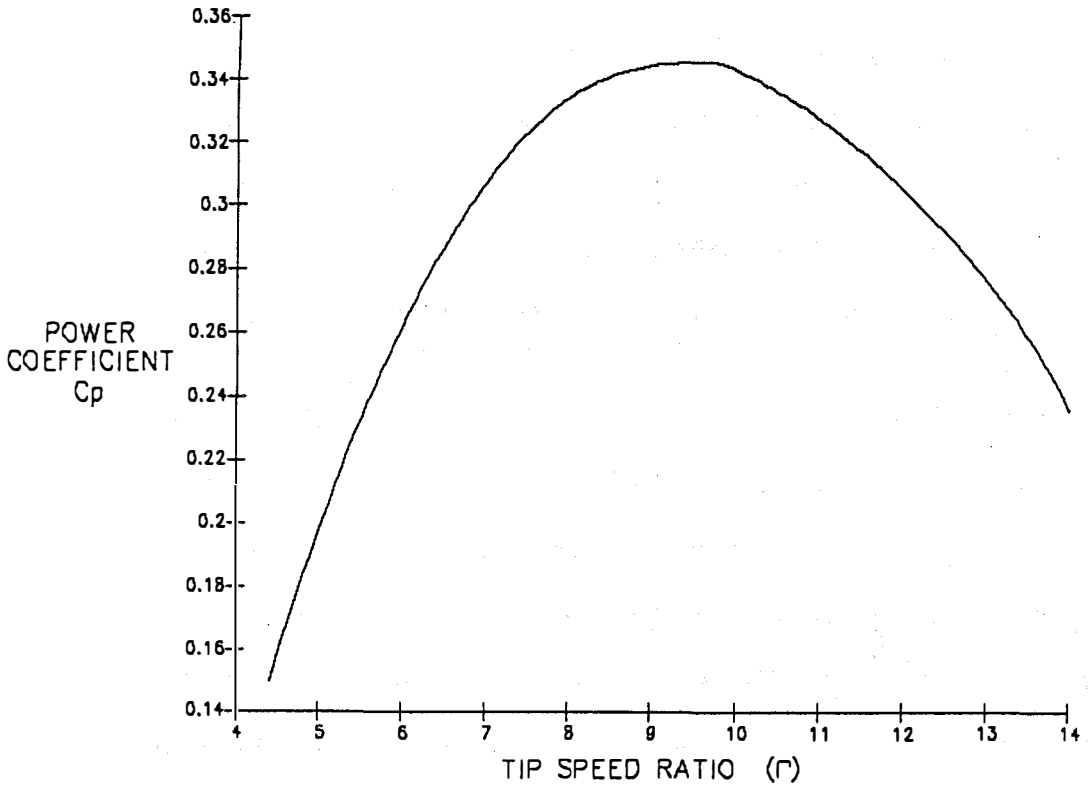

Figure 1.1 Typical HAWT Power Coefficient Curve.

advantages for wind farms with a large number of turbines; when a wind gust occurs, a large, potentially damaging voltage spike could be sent through the utility distribution system. The direct variation of torque with wind tends to decrease the fatigue life of the drive-train components. Variable-speed machines can use the rotor as a flywheel storage system to reduce these effects. When a wind gust is experienced the rotor can accelerate, transferring the increase in wind energy to the rotor as kinetic energy instead of passing it down the drive train as a sudden increase in torque. During a wind deficit the opposite effect occurs. The generator extracts energy from the rotor, which will decelerate the rotor. This process significantly dampens torque variations due to turbulence, tower shadow, and wind shear.

The variable-speed configuration can be used as a turbine control system. Many fixed-pitch machines use blade pitching to keep thrust and torque below some nominal value dictated by machine limitations. Instead, the rotor speed can be varied to achieve the same result without the complicated pitch actuators. Control schemes using both variable-speed generators and mechanical blade pitching were developed for HAWT [12-13]. Blade pitching reduces torque variations while maintaining rated power.

Variable-speed generators can be used to regulate start and stop conditions. Turbines can be motored to a start-up rotation speed, and braking can be achieved by setting the generator electrical torque higher than the mechanical rotor torque. Braking ability would still be needed for emergency loss of load. Some fixed-speed machines freewheel up to their normal operating speed and the generator is then turned on. This causes an impulse torque to be transmitted through the drive train increasing wear and fatigue. Fixed-speed machines need a braking device to stop the turbine. Brakes are aerodynamic, such as blade feathering, or mechanical, such as friction brakes. Anderson et al. [10] were able to use motored start up to 67% of rated rotor speed for a 500-horsepower variable-speed demonstration. The start up took approximately 100 seconds.

Variable-speed generators can be used to dampen out torsional modes that exist in the drive train. This phenomenon is often referred to as ringing. The quick response of generator torque allows damping of very high modes. A simulated 0.1 Hertz drive train resonance was successfully damped out on a 500-horsepower variable-speed demonstration [10].

The problem of synchronizing wind turbine output power with the utility is eliminated with variable-speed operation. This reduces the amount of time the generator is off line during start-up conditions. This can be significant when the wind is oscillating around the minimum operating speed.

Variable-speed operation can also reduce acoustic noise. Noise reduction is important when the turbines are sited near residential areas. At high wind speeds the rotor is operating slower to limit torque. The slower rotor speed reduces the noise emitted by the blade.

The preceding paragraphs have outlined the many advantages of operating HAWTs with variable-speed generators. A number of variable-speed test machines have been built to date.

The MOD-0A, a two-bladed HAWT, was equipped with a variable-speed generator and tested in a number of configurations [14]. Drive train load variations were reduced and the power quality was improved with the variable-speed operation.

A three-bladed 40-kiloWatt HAWT was tested in Sweden [15] with a constant tip-speed ratio below rated torque. Significant torque variations were reduced with the variable-speed generator.

Other test variable speed HAWTs have been studied in Japan [16], Germany [17], and Italy [18]. At the German site, noise reduction was reported for the variable-speed operation.

1.2 Blade Dynamics

The blades of a HAWT are long cantilever beams. The blades are frequently rigidly attached to the hub. The hub can either be rigidly attached to the low-speed shaft or allowed to teeter. Teeter mechanisms can include the displacement of the teeter axis from the blades principal bending axes, which is referred to as undersling, and the teeter axis may be rotated from a perpendicular alignment from the blades, referred to as a delta-3 angle. Each blade has three degrees of freedom: motion in the flapping direction, motion in the edgewise direction, and torsional motion. A teetered rotor would have seven degrees of freedom, three for each blade and one for the teeter motion. This geometry is similar to that of many helicopter rotors. One major difference is that helicopter blades are kept as light as possible to reduce power required for flight. Helicopter blades are also replaced frequently, as often as every 1000 hours of flight time, resulting in less required structural support to resist fatigue. Conse-

quently, most HAWT blades are much heavier and stiffer than helicopter blades. Most of the governing equations for blade motions are similar. The large difference in stiffness results in some of the terms governing HAWT blade motion to be small. The torsional stiffness can be more than an order of magnitude greater than the edgewise stiffness, which in turn may be an order of magnitude greater than the flapwise stiffness. Often, the degrees of freedom in these directions can be ignored. A thorough description of governing equations for blade motion can be found in Johnson [19], Bramwell [20], and Gessow and Meyers [21]. A discussion of current blade modeling techniques is made by Hodges [22]. Solutions to the blade equations can be found depending on their complexity. Aeroelastic solutions can be obtained by linearizing the dynamics and the aerodynamics. This technique is more suitable for helicopters, where the geometry lends itself to linearization. In the literature, a number of researchers have examined aeroelastic solutions for helicopter rotors [23-25]. Kottapalli and Friedman [26] examined the aeroelastic stability of a wind turbine blade by computing an equilibrium position for the nonlinear equations and then examining the behavior of perturbations about the equilibrium position. Linearized dynamics has been used to examine system natural frequencies and stability regions [27-28]. Including the nonlinearities in the dynamics and the aerodynamics requires a solution in the time domain. Recently, Hartin [4] combined tower motion and elastic blade flapping with an unsteady aerodynamic model for a HAWT. The response was obtained by using a time domain predictor-corrector method.

1.3 Rotary Wing Aerodynamics

Aerodynamic loads on a HAWT rotor are determined using the axial momentum theory for an actuator disk, which was first examined by Rankine [29] and Froude [30]. This theory balances the thrust from the momentum change of the flow passing through rotor with the blade element thrust. This theory is often referred to as strip theory as the flow through the rotor can be divided up into individual stream tubes or "strips." This theory was modified by Prandtl [31] and Goldstein [32] to account for tip-loss effects. A modified strip theory was developed by Wilson and Walker [33] to account for wake expansion. Using the assumption of linear aerodynamics, closed-form solutions can be achieved. Most

HAWTs operate with large portions of their blades in deep stall, so use of linear aerodynamics is not generally a valid assumption. When nonlinear aerodynamics is used, a solution can be found through an iterative procedure. The inclusion of nonlinear aerodynamics has been shown to be an improvement [34].

A wind model to drive the aerodynamic model consists of two distinct parts: a deterministic part and a stochastic part. The deterministic wind consists of effects that are repeated for each rotor revolution. These are the mean wind, wind shear, tower interference, and yaw. The stochastic portion is due to atmospheric turbulence. Turbulence consists of lateral, vertical, and longitudinal components. Only the longitudinal component is important in HAWT load analysis. Many turbulence models have been developed using simple autoregression for a single point in space. Connell [35] developed a model that decomposes a Fourier Transform of a autocorrelation for a rotating point in turbulent wind, which can be used for analysis of a small HAWT with a rigid rotor. Veers [36] developed a full-field model that has many applications in wind engineering but requires mainframe memory to run. Walker et al. [37] summarized turbulence models for HAWT use. A number of analysts have implemented turbulence models into load prediction codes [38-40].

2. DEVELOPMENT OF EQUATIONS OF MOTION

Four degrees of freedom are necessary to model a HAWT with a two-bladed, teetered hub connected to a variable-speed generator. One degree of freedom arises from the flapwise motion of each of the two blades. Motion of the blade is confined to the flapwise direction. Edgewise and torsional blade motion are not considered in this study. The direction of the blade flapping is a function of the twist and pitch of the blade, so that the motion is in the direction perpendicular to the axis of the blades' smallest moment of inertia. The model allows for blade precone and delta-3. The model also allows for the teetering hub center to be offset from the teeter axis. This length is referred to as under-sling. The model has provisions for fixed-rotor tilt and yaw. Time-varying yaw is not considered. The variable-speed generator is driven by the aerodynamic torque, drive train losses, and an arbitrary generator load. The aerodynamic loading is determined using the modified strip theory with nonlinear lift and drag characteristics. The aerodynamics are driven by a wind model that consists of a deterministic portion made up of mean wind, shear, and yaw, and a stochastic portion, consisting of an atmospheric turbulence model. The aerodynamic loads are calculated in the deformed blade position. The resulting nonlinear equations are solved in the time domain using a predictor-corrector method. The bending moments, shear, and tension forces are integrated along the deformed blade. The derivation of the governing equations of motion is presented in this chapter.

2.1 Geometry and Coordinate Transformations

Figure 2.1 shows the orientation of one turbine blade with all the coordinate systems required for determination of the system equations of motion. These coordinates are defined as:

$\mathbf{a}_i''$ = inertial coordinates

$\mathbf{a}_i'$ = yaw coordinates

$\mathbf{a}_i$ = tilt and generator coordinates

$\mathbf{b}_i$ = rotating rotor coordinates

$\mathbf{c}_i$ = rotating teeter coordinates

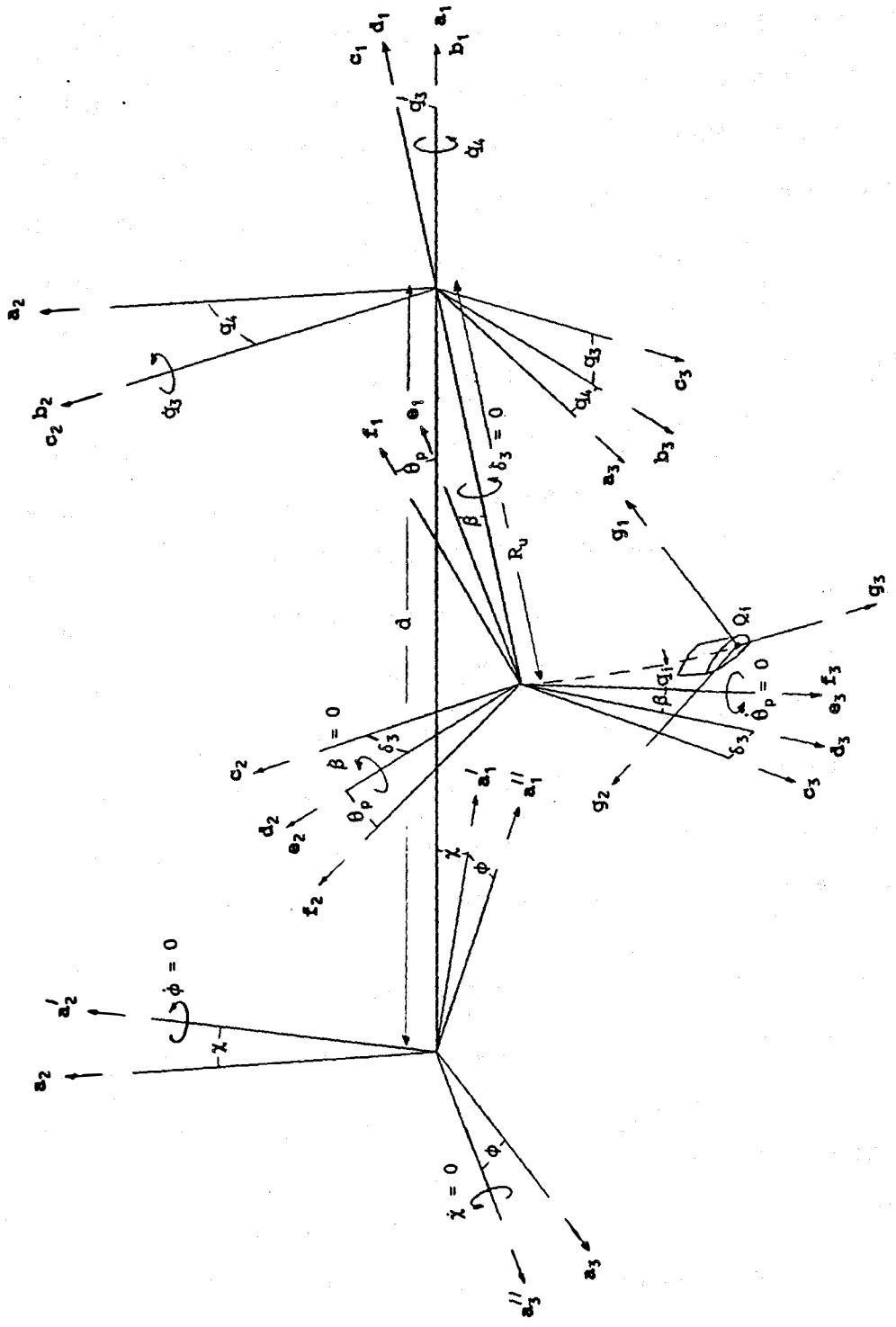

Figure 2.1. Rotor Coordinate System.

$\mathbf{d}_i$ = delta-3 rotation coordinates

$\mathbf{e}_i$ = precone rotation coordinates

$\mathbf{f}_i$ = elastic axis rotation coordinates

$\mathbf{g}_i$ = deflected blade coordinates

(i=1,2,3)

The first two coordinate transformations, $\mathbf{a}''$ to $\mathbf{a}'$ and $\mathbf{a}'$ to $\mathbf{a}$, are yaw and tilt rotations respectively, and are used to determine wind input. The tilt rotation also affects the gravity load on the rotor. The rotor generator and main shaft spin about the $\mathbf{a}_1$ axis. The rotation about this axis is the variable-speed degree of freedom, q_4. The rotor assembly teeters about the $\mathbf{b}_2$ axis, with the teeter axis being displaced from the yaw and tilt axes' center by a distance, d. The rotation about the teeter axis is the teeter degree of freedom, q_3. The hub is displaced from the teeter axis by the undersling distance, R_u. The axes $\mathbf{c}_1$, $\mathbf{d}_2$, and $\mathbf{e}_3$ define rotations at the hub center for delta-3 (δ_3), precone (β), and the elastic bending axis (Θ_p), respectively. The resulting coordinate transformation from the generator coordinate system to the rigid blade coordinate system is given by:

$$\begin{Bmatrix} a_1 \\ a_2 \\ a_3 \end{Bmatrix} = \begin{bmatrix} Q^{11} & Q^{12} & Q^{13} \\ Q^{21} & Q^{22} & Q^{23} \\ Q^{31} & Q^{32} & Q^{33} \end{bmatrix} \begin{Bmatrix} f_1 \\ f_2 \\ f_3 \end{Bmatrix} \qquad (2.1.1)$$

where,

$$
\begin{aligned}
Q^{11} &= c\theta_p c\beta c q_3 + s\theta_p s\delta_3 s q_3 - c\theta_p s\beta c\delta_3 s q_3 \\
Q^{12} &= -s\theta_p c\beta c q_3 + c\theta_p s\delta_3 s q_3 + s\theta_p s\beta c\delta_3 s q_3 \\
Q^{13} &= s\beta c q_3 + c\beta c\delta_3 s q_3 \\
Q^{21} &= c\theta_p c\beta s q_3 s q_4 + s\theta_p Q^A + c\theta_p s\beta Q^B \\
Q^{22} &= -s\theta_p c\beta s q_3 s q_4 + c\theta_p Q^A - s\theta_p s\beta Q^B \\
Q^{23} &= s\beta s q_3 s q_4 - c\beta(s\delta_3 c q_4 + c\delta_3 c q_3 s q_4) \\
Q^{31} &= -c\theta_p c\beta s q_3 c q_4 + s\theta_p Q^C - c\theta_p s\beta Q^D \\
Q^{32} &= s\theta_p c\beta s q_3 c q_4 + c\theta_p Q^C + s\theta_p s\beta Q^D \\
Q^{33} &= -s\beta s q_3 c q_4 + c\beta(-s\delta_3 s q_4 + c\delta_3 c q_3 c q_4) \\
Q^A &= c\delta_3 c q_4 - s\delta_3 c q_3 s q_4 \\
Q^B &= s\delta_3 c q_4 + c\delta_3 c q_3 s q_4 \\
Q^C &= c\delta_3 s q_4 + s\delta_3 c q_3 s q_4 \\
Q^D &= -s\delta_3 s q_4 + c\delta_3 c q_3 c q_4
\end{aligned}
\tag{2.1.2}
$$

($\cos(q_4)$ is written as cq_4, $\sin(q_4)$ as sq_4, and so on for brevity).

For determining aerodynamic loads, the transformation from rigid blade coordinates to the deformed blade coordinates can be taken as a local rotation about the $\mathbf{f}_2$ axis. This must be done for each blade element with a rotation ζ. The transformation between the rigid and deformed blade coordinates is given by:

$$
\begin{Bmatrix} f_1 \\ f_2 \\ f_3 \end{Bmatrix} = \begin{bmatrix} \cos(\zeta) & 0 & -\sin(\zeta) \\ 0 & 1 & 0 \\ \sin(\zeta) & 0 & \cos(\zeta) \end{bmatrix} \begin{Bmatrix} g_1 \\ g_2 \\ g_3 \end{Bmatrix} \tag{2.1.3}
$$

2.2 Blade Deflection

The displacement of each blade is modeled as a single degree of freedom in a direction perpendicular to the axis of the blades smallest moment of inertia. This is not necessarily perpendicular to the swept rotor plane due to twist and pitch. Blade deflection tangential to the axis of the smallest moment of inertia is zero, although provisions have been left in the code for future development. Deflection in the radial direction can be expressed as a function of the flapwise displacement. Displacement of the blade is given by a product of an assumed mode shape and a function of time. This relation for displacement in the flapwise or f_1 blade coordinate direction can be expressed as:

$$u_{1i} = \phi_1(r)q_i(t) \qquad (i = 1,2) \tag{2.2.1}$$

where,

$q(t)$ = the blade displacement, a function of time

$\phi_i(r)$ = the assumed mode shape, a function of the blade coordinate r.

i = blade number (i = 1,2)

The displacement in the tangential or f_2 blade coordinate can be expressed in the same manner as:

$$u_{2i} = \phi_2(r)q_i(t) \qquad (i=1,2) \tag{2.2.2}$$

For this model the assumed mode shape $\phi_2(r)$ is zero for all values of r.

For a small blade deflection as shown in Figure 2.2, the radial deflection can be expressed as:

$$u_{3i} = \int_0^r \cos\left(\frac{\partial u_{1i}}{\partial r}\right) dr \qquad (i=1,2) \tag{2.2.3}$$

Taking the first two terms from a Taylor series of the cosine function and linearizing gives:

$$\cos\left(\frac{\partial u_i}{\partial r}\right) = 1 - 2\sin^2\frac{\partial u_i}{\partial r} \approx 1 - \frac{1}{2}\left(\frac{\partial u_i}{\partial r}\right)^2 \tag{2.2.4}$$

so that:

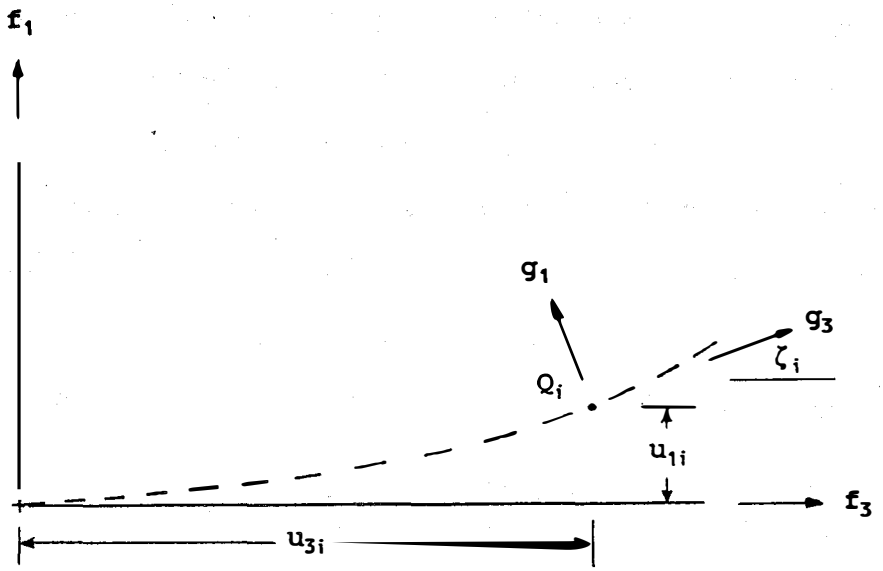

Figure 2.2. Blade Deflection

$$u_{3i} = r - \frac{1}{2} q_i^2 \int_o^r \left(\frac{\partial \phi_i}{\partial r} \right)^2 dr \qquad (i=1,2) \tag{2.2.5}$$

The local blade element rotation used for Eq. (2.1.3) can be approximated as the slope of the displacement function given as:

$$\zeta_i(r) = q_i(t) \frac{\partial \phi_1}{\partial r} \qquad (i=1,2) \tag{2.2.6}$$

The choice for the shape function was determined using the following relation developed by Wilson et al. [1] for an Euler beam that has stiffness that varies as:

$$EI = kr^{-b} \tag{2.2.7}$$

where k is a constant, r is the distance from the fixed hub, and $b \geq 0$. For a uniformly loaded cantilevered beam with stiffness variation as given in Eq. (2.2.6), the static deflection (normalized to unity at the blade tip) is given by:

$$\phi_a(z) = \frac{z^{b+2}}{6}\left[(1+b)(2+b)z^2 - 2(1+b)(4+b)z + (3+b)(4+b)\right] \tag{2.2.8}$$

where $z = (r-R_H)/(R-R_H)$, R is the length of the blade, and R_H is the hub length. For a cantilevered beam with a force acting at the tip and the stiffness given in Eq. (2.2.6), the static deflection (normalized to unity at the tip) is given by:

$$\phi_b(z) = \frac{z^{b+2}}{2}\left[(3+b) - (1+b)z\right] \tag{2.2.9}$$

For a cantilevered beam with a uniform load and a force acting at the tip (i.e., a tip mass), the relation for the static deflection is a weighted superposition of Eqs. (2.2.8) and (2.2.9), written as:

$$\phi(z) = w\phi_a(z) + (1-w)\phi_b(z) \tag{2.2.10}$$

where w is a weighting factor between one and zero. Wilson and Hartin [41] found that the parameter b could be found by calculating the bending natural frequency for a range of values of b and selecting the value of b that minimizes the flapwise bending frequency. This procedure can be extended to find a combination of values w and b that minimizes the bending natural frequency. For the ESI-80, the turbine used for comparison in this study and described in the DRT user's guide [42], minimizing values were found to be 1.3 for b and 0 for w. These values were used for the rest of the analysis.

2.3 Blade Kinematics

Expressions for the velocity and acceleration of an arbitrary point on the blade is required for determining blade equations of motion and blade forces. A position vector of an arbitrary point Q on the i^{th} deformed blade can be written as:

$$\left({}^N\boldsymbol{p}^Q\right)_i = p_{1i}\boldsymbol{f}_1 + p_{2i}\boldsymbol{f}_2 + p_{3i}\boldsymbol{f}_3 \qquad (i=1,2) \tag{2.3.1}$$

where,

$$p_{1i} = u_{1i} - R_U\cos(\beta)$$

$$p_{2i} = u_{2i} \tag{2.3.2}$$

$$p_{3i} = u_{3i} - R_U\sin(\beta) \qquad (i=1,2)$$

where $({}^N\mathbf{p}^Q)_i$ is the position vector of a point Q in the inertial reference frame N. The displacements u_{1i}, u_{2i}, and u_{3i} are given in Eqs. (2.2.1), (2.2.2), and (2.2.5), respectively. The velocity of the point Q is the time derivative of the position vector in (2.3.1) given by:

$$({}^N\boldsymbol{v}^Q) = \left(\frac{({}^N\mathrm{d}\ {}^N\boldsymbol{p}^Q)}{\mathrm{dt}}\right) \tag{2.3.3}$$

This can be expressed in the rigid blade coordinate as:

$$({}^N\boldsymbol{v}^Q)_I = v_{1i}\boldsymbol{f}_1 + v_{2i}\boldsymbol{f}_2 + v_{3i}\boldsymbol{f}_3 \tag{2.3.4}$$

where,

$$\begin{aligned} v_{1i} &= \dot{u}_{1i} + (w_2p_{3i} - w_3p_{2i}) \\ v_{2i} &= \dot{u}_{2i} + (w_3p_{1i} - w_1p_{3i}) \\ v_{3i} &= \dot{u}_{3i} + (w_1p_{2i} - w_2p_{1i}) \end{aligned} \tag{2.3.5}$$

where,

$$\begin{aligned} \dot{u}_{1i} &= \dot{q}_i\phi_1 \\ \dot{u}_{2i} &= \dot{q}_i\phi_2 = 0 \\ \dot{u}_{3i} &= -\dot{q}_i\, q_i \int_0^r \left(\frac{\partial\phi}{\partial r}\right)^2 dr \qquad (i=1,2) \end{aligned} \tag{2.3.6}$$

and,

$$\begin{aligned} w_1 &= \dot{q}_4 Q^{11} + \dot{q}_3(\cos(q_4)Q^{21} + \sin(q_4)Q^{31}) \\ w_2 &= \dot{q}_4 Q^{12} + \dot{q}_3(\cos(q_4)Q^{22} + \sin(q_4)Q^{32}) \\ w_3 &= \dot{q}_4 Q^{13} + \dot{q}_3(\cos(q_4)Q^{23} + \sin(q_4)Q^{33}) \end{aligned} \tag{2.3.7}$$

where q_3 and q_4 are the teeter and variable-speed degrees of freedom, respectively, and $\dot{q}_3$ and $\dot{q}_4$ are their time derivatives. Q^{11} through Q^{33} are transformations given in Eq. (2.1.1).

The acceleration of point Q is the time derivative of the velocity vector given in Eq. (2.3.4) given by:

$$({}^N\boldsymbol{a}^Q) = \left(\frac{({}^N\boldsymbol{d}\,{}^N\boldsymbol{V}^Q)}{dt}\right) \tag{2.3.8}$$

This can be expressed in the rigid blade coordinates as:

$$({}^N\boldsymbol{a}^Q)_I = a_{1i}\boldsymbol{f}_1 + a_{2i}\boldsymbol{f}_2 + a_{3i}\boldsymbol{f}_3 \tag{2.3.9}$$

where (ignoring the indice i),

$$\begin{aligned} a_1 &= \ddot{u}_1 + 2(w_2\dot{u}_3 - w_3\dot{u}_2) + (w_2v_3 - w_3v_2) + (\alpha_2p_3 - \alpha_3p_2) \\ a_2 &= \ddot{u}_2 + 2(w_3\dot{u}_1 - w_1\dot{u}_3) + (w_3v_1 - w_1v_3) + (\alpha_3p_1 - \alpha_1p_3) \\ a_3 &= \ddot{u}_3 + 2(w_1\dot{u}_2 - w_2\dot{u}_1) + (w_1v_2 - w_2v_1) + (\alpha_1p_2 - \alpha_2p_1) \end{aligned} \tag{2.3.10}$$

where w_1, w_2, and w_3 are given in Eq. (2.3.7); v_1, v_2, and v_3 are given in Eq. (2.3.5); and u_1, u_2, and u_3 are given in Eq. (2.3.6), and:

$$\begin{aligned} \ddot{u}_{1i} &= \ddot{q}_i\phi_1 \\ \ddot{u}_{2i} &= \ddot{q}_i\phi_2 = 0 \\ \ddot{u}_{3i} &= -(\ddot{q}_i + (\dot{q}_i)^2)\int_0^r \left(\frac{\partial\phi}{\partial r}\right)^2 dr \end{aligned} \tag{2.3.11}$$

and,

$$
\begin{aligned}
\alpha_1 &= \ddot{q}_4 Q^{11} + \ddot{q}_3 Q^{W1} + \dot{q}_3 \dot{q}_4 Q^{A1} \\
\alpha_2 &= \ddot{q}_4 Q^{12} + \ddot{q}_3 Q^{W2} + \dot{q}_3 \dot{q}_4 Q^{A2} \\
\alpha_3 &= \ddot{q}_4 Q^{13} + \ddot{q}_3 Q^{W3} + \dot{q}_3 \dot{q}_4 Q^{A3} \\
Q^{W1} &= \cos(q_4) Q^{21} + \sin(q_4) Q^{31} \\
Q^{W2} &= \cos(q_4) Q^{22} + \sin(q_4) Q^{32} \\
Q^{W3} &= \cos(q_4) Q^{23} + \sin(q_4) Q^{33} \\
Q^{A1} &= \cos(q_4) Q^{31} - \sin(q_4) Q^{21} \\
Q^{A2} &= \cos(q_4) Q^{32} - \sin(q_4) Q^{22} \\
Q^{A3} &= \cos(q_4) Q^{33} - \sin(q_4) Q^{23}
\end{aligned}
\tag{2.3.12}
$$

the $\ddot{q}$'s are the second time derivatives of the q's and Q^{11} through Q^{33} are transformation given in Eq. (2.1.1). The angular velocity can be written using Eq. (2.3.7) as:

$$
({}^N w^Q) = w_1 f_1 + w_2 f_2 + w_3 f_3 \tag{2.3.13}
$$

The angular acceleration can be written using Eq. (2.13.12) as:

$$
({}^N \alpha^Q) = \alpha_1 f_1 + \alpha_2 f_2 + \alpha_3 f_3 \tag{2.3.14}
$$

2.4 Aerodynamic Loading

The method for determining aerodynamic loads is based on the momentum theory. The momentum theory applies continuity, momentum, and energy to the flow passing through the rotor plane. Figure 2.3 shows the one-dimensional flow past the rotor. Two expressions for the thrust on the rotor can be found. From a conservation of momentum:

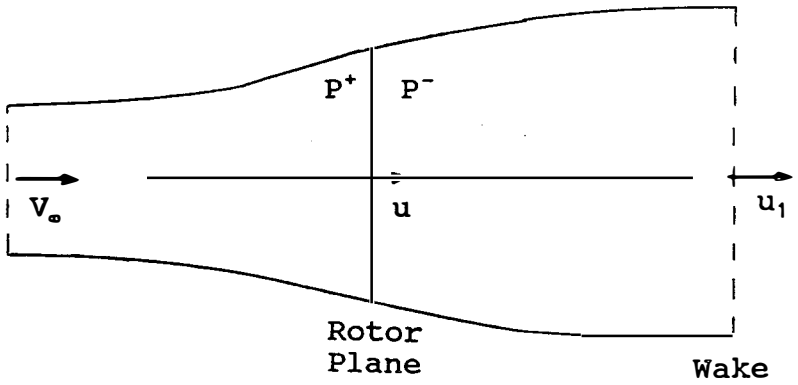

Figure 2.3. One-Dimensional Flow Past Rotor.

$$\frac{dT}{dA} = \rho u(V_\infty - u) \tag{2.4.1}$$

where dT/dA is the axial force per unit area on the actuator disk, ρ is the fluid density, and V_∞ and u are velocities defined on Figure 2.3. From the Bernoulli equation:

$$\frac{dT}{dA} = \Delta P \tag{2.4.2}$$

where ΔP is the pressure difference across the actuator disk expressed as:

$$\Delta P = P^+ - P^- = \frac{1}{2}\rho\left(V_\infty^2 - u_1^2\right) \tag{2.4.3}$$

Solving Eqs. (2.4.1) and (2.4.2) gives the velocity in the rotor disk as:

$$u = \frac{1}{2}(V_\infty + u_1) \tag{2.4.4}$$

Defining a as the axial induction factor through the relation $aV_\infty = V_\infty - u$ the momentum relation Eq. (2.4.1) can be written as:

$$\frac{dT}{dA} = 2\, V_\infty^2\, a\, (1 - a) \tag{2.4.5}$$

By defining the rotor thrust coefficient as:

$$C_T = \frac{\frac{dT}{dA}}{\frac{1}{2}\, \rho\, V_\infty^2} \tag{2.4.6}$$

the thrust coefficient can be expressed as a function of the axial induction factor:

$$C_T = 4\, a\, (1 - a) \tag{2.4.7}$$

The effect of the wake expansion on the thrust coefficient was studied by Glauret both empirically [43] and analytically [44]. The following expression given by Wilson and Walker [33] can be used to specify the thrust coefficient:

$$\begin{aligned} C_T &= 4\, a\, F\, (1 - a) && a \le a_c \\ C_T &= C_{T_{ac}} + \left.\frac{\partial C_T}{\partial a}\right|_{ac} (a - a_c) && a > a_c \end{aligned} \tag{2.4.8}$$

A value of $a_c = 0.2$ gives the best fit to the data. F is a tip-loss factor, given by Prandtl [31] as follows

$$F = \frac{2}{\pi} \cos^{-1} \left[\exp \frac{-B\, (R - r)}{2\, \pi\, r \sin\phi_\alpha} \right] \tag{2.4.9}$$

Strip theory combines the momentum theory with a blade element theory and is based on the assumption that the flow through the rotor can be divided into individual stream tubes that can be analyzed independently. The advantage of strip theory is that the axial induction factors can be found for each element independently of one another. The thrust relation Eq. (2.4.8) can be related to the blade element thrust coefficient, which is given as follows:

$$C_T = \frac{B\ c\ (1 - a)^2\ C_L \cos\phi_\alpha}{2\ \pi\ r \sin^2\phi_\alpha} \tag{2.4.10}$$

where,

$$\phi_\alpha = \tan^{-1} \frac{V_\infty\ (1 - a)}{r\Omega} \tag{2.4.11}$$

A solution to Eqs. (2.4.8), (2.4.10), (2.4.11), and (2.4.12) can be found in an iterative manner to give the steady-state axial induction factor. This allows the lift and drag to be determined along the blade for any blade azimuth location, as follows:

$$\begin{aligned} \text{Lift / (unit length)} &= \frac{1}{2}\ \rho\ W^2\ c\ C_L \\ \text{Drag / (unit length)} &= \frac{1}{2}\ \rho\ W^2\ c\ C_D \end{aligned} \tag{2.4.13}$$

Referring to the geometry of Figure 2.4, the lift and drag can be resolved onto the blade coordinates such that the aerodynamic forces acting on a blade element can be written as:

$$\boldsymbol{f} = f_n \boldsymbol{f}_1 + f_t \boldsymbol{f}_2 \tag{2.4.14}$$

where,

$$\begin{aligned} f_n &= L \cos\phi_\alpha + D \sin\phi_\alpha \\ f_t &= -\ L \sin\phi_\alpha + D \cos\phi_\alpha \end{aligned} \tag{2.4.15}$$

where, L = lift, and D = drag.

2.5 Equations of Motion

The kinematics and forces are evaluated at discrete points along the blades so that determination of the equations of motion requires numeric integration along the blades. The methods of Kane and Levinson [45] were used for obtaining the equations of motion. The equations are of the form:

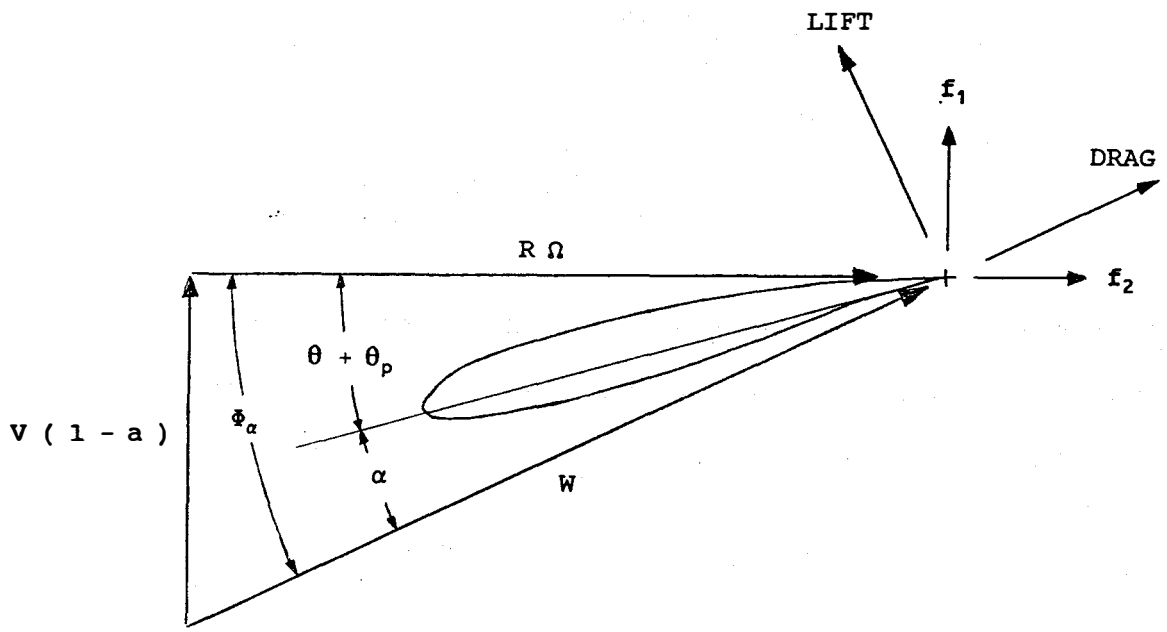

Figure 2.4. Airfoil Velocities.

$$F_r + F_r^* = 0 \tag{2.5.1}$$

where,

F_r = generalized active force

F_r^* = generalized inertia force

The subscript r refers to the number of generalized coordinates. In this model, the number of generalized coordinates is equivalent to the number of degrees of freedom. As defined in section 2.1, r=1 and r=2 correspond to the blade deflections of the two blades; r=3 for the teeter angle, and r=4 for the variable speed. The generalized active forces are determined from the blade kinematics using:

$$F_r = \boldsymbol{V}_r^Q \cdot \boldsymbol{R} + \omega_r^Q \cdot \boldsymbol{T} \qquad r=1,4 \tag{2.5.3}$$

where,

$\mathbf{V}_r^Q$ = holonomic partial velocity of point Q

$\mathbf{R}$ = resultant of all external force

$\boldsymbol{\omega}_r^Q$ = holonomic partial angular velocity of point Q

$\mathbf{T}$ = resultant torque of all external torques

The generalized inertia forces are determined using the following relation:

$$F_r^* = \boldsymbol{V}_r^Q \cdot (-\, m\, \boldsymbol{a}^Q) + \boldsymbol{\omega}_r^Q \cdot (-\, \boldsymbol{\alpha} \cdot \boldsymbol{I} - \boldsymbol{\omega} \times \boldsymbol{I} \cdot \boldsymbol{\omega}) \qquad r=1,4 \qquad (2.5.3)$$

where,

m = mass per unit length of the blade

$\mathbf{a}^Q$ = acceleration of point Q, Eq. (2.3.9)

$\mathbf{I}$ = Inertia dyadic of blade element Q

$\boldsymbol{\alpha}$ = angular acceleration of point Q, Eq. (2.3.14)

$\boldsymbol{\omega}$ = angular velocity of point Q, Eq. (2.3.13)

The generalized speeds are defined as $u_r=\dot{q}_r$ (r=1,4). The partial velocities can be found from the expression for blade velocity, Eq. (2.3.5):

$$\begin{aligned}
\boldsymbol{V}_r^{Q_j} &= \phi_{1r}\boldsymbol{f}_1 + \phi_{2r}\boldsymbol{f}_2 - q_r \int_0^r \left(\frac{\partial \phi}{\partial r}\right)^2 dr\boldsymbol{f}_3 && j = r \\
\boldsymbol{V}_r^{Q_j} &= 0 && j \neq r \;;\; r = 1,2 \\
\boldsymbol{V}_3^{Q_j} &= N_{31}^j \boldsymbol{f}_1 + N_{32}^j \boldsymbol{f}_2 + N_{33}^j \boldsymbol{f}_3 && r = 1,2 \\
\boldsymbol{V}_4^{Q_j} &= N_{41}^j \boldsymbol{f}_1 + N_{42}^j \boldsymbol{f}_2 + N_{43}^j \boldsymbol{f}_3 && r = 1,2
\end{aligned} \qquad (2.5.4)$$

where,

$$
\begin{aligned}
N_{31} &= Q^{W2}P_3 - Q^{W3}P_2 \\
N_{32} &= Q^{W3}P_1 - Q^{W1}P_3 \\
N_{33} &= Q^{W1}P_2 - Q^{W2}P_1 \\
N_{41} &= Q^{12}P_3 - Q^{13}P_2 \\
N_{42} &= Q^{13}P_1 - Q^{11}P_3 \\
N_{43} &= Q^{11}P_2 - Q^{12}P_1
\end{aligned}
\tag{2.5.5}
$$

The partial angular velocities can be found from the expression for blade angular velocity, Eq. (2.3.13):

$$
\begin{aligned}
\omega_r^{Q_j} &= 0 \qquad\qquad r = 1,2 \\
\omega_3^{Q_1} &= \boldsymbol{b}_2 \\
\omega_3^{Q_2} &= -\boldsymbol{b}_2 \\
\omega_4^{Q_j} &= \boldsymbol{a}_1 \qquad\qquad j = 1,2
\end{aligned}
\tag{2.5.6}
$$

The resultant **R** can be written as a combination of aerodynamic Eq. (2.4.5) and gravity forces:

$$
\boldsymbol{R} = R_1\boldsymbol{f}_1 + R_2\boldsymbol{f}_2 + R_3\boldsymbol{f}_3 \tag{2.5.7}
$$

where,

$$
\begin{aligned}
R_1 &= -m\,g\,(\cos(\chi)Q^{21} - \sin(\chi)Q^{11}) + f_n \\
R_2 &= -m\,g\,(\cos(\chi)Q^{22} - \sin(\chi)Q^{12}) + f_t \\
R_3 &= -m\,g\,(\cos(\chi)Q^{23} - \sin(\chi)Q^{13})
\end{aligned}
\tag{2.5.8}
$$

The resultant torque **T** is due solely to that of the restraining torque of the generator. The generator model is discussed in section 2.6. The relation for the generalized inertia forces can be taken as:

$$F_r^* = -\sum_{j=1}^{2} \left(\int_0^R \mu \, \boldsymbol{V}_r^{Q_j} \cdot \boldsymbol{a}^{Q} \, dr \right) \qquad r = 1,4 \tag{2.5.9}$$

This relation can be expanded into a form where the second time derivatives are extracted so that the equations can be written in the form:

$$[\boldsymbol{M}]\{\ddot{\boldsymbol{q}}\} = \{\boldsymbol{G}\} \tag{2.5.10}$$

This form lends itself to a predictor-corrector scheme for solution of the equations. With this in mind, the first two generalized inertia forces can written as:

$$\begin{aligned} F_r^* = & -\ddot{q}_r \int_0^R \mu \left(\phi_1^2 + \left(q_r \int_0^r \left(\frac{\partial \phi}{\partial \bar{r}} \right)^2 d\bar{r} \right)^2 \right) dr \\ & -\ddot{q}_3 \int_0^R \mu \left[(Q^{W2}P_3 - Q^{W3}P_2)\phi_1 + (Q^{W1}P_2 - Q^{W2}P_1)\phi_3 \right] dr \\ & -\ddot{q}_4 \int_0^R \mu \left[(Q^{12}P_3 - Q^{13}P_2)\phi_1 + (Q^{11}P_2 - Q^{12}P_1)\phi_3 \right] dr \\ & -g_r(q_i, \dot{q}_i) \qquad r = 1,2 \qquad i = 1,4 \end{aligned} \tag{2.5.11}$$

where,

$$\begin{aligned} \phi_3 &= \left(-\int_0^r \left(\frac{\partial \phi}{\partial \bar{r}} \right)^2 d\bar{r} \right) \\ g_r(q_i, \dot{q}_i) &= \dot{q}_3 \, \dot{q}_4 \int_0^R \mu \left[(Q^{A2}P_3 - Q^{A3}P_2)\phi_1 + (Q^{A1}P\text{-}2 - Q^{A2}P_1)\phi_3 \right] dr \\ &\quad - \int_0^R \mu \left[(W_2V_3 - W_3V_2)\phi_1 + (W_1V_2 - W_2V_1)\phi_3 + \dot{q}_r^2 \phi_3 \right] \\ &\quad r = 1,2 \end{aligned} \tag{2.5.12}$$

The second two generalized inertia forces can be written as:

$$
\begin{aligned}
F_r^* = -\sum_{j=1}^{2} \Big[& \ddot{q}_j \int_0^R \mu \left(\phi_1 N_{r1}^j + \phi_3 N_{r3}^j\right) dr + \frac{1}{2} I_{generator}\, \ddot{q}_4 \quad (if\ r=4) \\
& -\ddot{q}_3 \int_0^R \mu \left[(Q^{W2}P_1 - Q^{W3}P_2)N_{r1} + (Q^{W3}P_1 - Q^{W1}P_3)N_{r2} + (Q^{W1}P_2 - Q^{W2}P_1)N_{r3}\right] dr \\
& -\ddot{q}_4 \int_0^R \mu \left[(Q^{12}P_3 - Q^{13}P_2)N_{r1} + (Q^{13}P_1 - Q^{11}P_3)N_{r2} + (Q^{11}P_2 - Q^{12}P_1)N_{r2}\right] dr \\
& -g_r(q_i, \dot{q}_i) \Big] \qquad r = 3,4 \quad i = 1,4
\end{aligned}
\tag{2.5.13}
$$

where,

$$
\begin{aligned}
g_r(q_i, \dot{q}_i) = & \dot{q}_3 \dot{q}_4 \int_0^R \left[(Q^{A2}P_3 - Q^{A3}P_2)N_{r1}^j + (Q^{A3}P_1 - Q^{A1}P_3)N_{r2}^j + (Q^{A1}P_2 - Q^{A2}P_1)N_{r3}^j\right] dr \\
& + 2 \int_0^R \left[(W_2\dot{U}_3 - W_3\dot{U}_2)N_{r1}^j + (W_3\dot{U}_1 - W_1\dot{U}_3)N_{r2}^j + (W_1\dot{U}_2 - W_2\dot{U}_1)N_{r3}^j\right] dr \\
& + \int_0^R \left[(W_2V_3 - W_3V_2)N_{r1}^j + (W_3V_1 - W_1V_3)N_{r2}^j + (W_1V_2 - W_2V_1)N_{r3}^j\right] dr \\
& + \dot{q}_j^2 \int_0^R \left(\phi_3 N_{r3}^j\right) dr \qquad r = 3,4 \quad j = 1,2 \\
& + \dot{q}_4^2 I_{generator} \quad (\text{If } r=4)
\end{aligned}
\tag{2.5.14}
$$

The first two generalized active forces can be written as:

$$
\begin{aligned}
F_r = \int_0^R \Bigg(& R_1\phi_1 + R_3\phi_3 - q_r \int_0^r EI \left(\frac{\partial^2 \phi}{\partial \bar{r}^2}\right)^2 d\bar{r} \\
& - q_r \int_0^r \dot{q}_4^2\, \mu \left(\frac{\partial \phi}{\partial \bar{r}}\right)^2 d\bar{r} \Bigg) dr \\
& r = 1,2
\end{aligned}
\tag{2.5.15}
$$

The second two terms arise from the relation between the potential and the generalized active force:

$$
F_r = -\frac{\partial V}{\partial q_r} \tag{2.5.16}
$$

where the potential for a blade element is given as:

$$V = \frac{1}{2}\int_0^r EI\left(\frac{\partial^2 u_1}{\partial \bar{r}^2}\right)^2 d\bar{r} + \frac{1}{2}\int_0^r \dot{q}_4^2\,\mu\left(\frac{\partial u_1}{\partial \bar{r}}\right)^2 d\bar{r} \tag{2.5.17}$$

The second two generalized active forces can be written as:

$$F_r = \sum_{j=1}^{2}\left[\int_0^R \left(R_1 N_{r1}^j + R_2 N_{r2}^j + R_3 N_{r3}^j\right) dr\right] + \boldsymbol{T}\cdot\omega_r^{a_j} \qquad r = 3,4 \tag{2.5.18}$$

where **T** is the generator restraining torque. The hub mass has a contribution to the third and fourth generalized active and inertia forces:

$$\begin{aligned}
F_{3_{HUB}} &= M_{HUB}\,R_U\,g\,(\cos\chi\cos q_3\sin q_4 + \sin\chi\sin q_3)\\
F_{4_{HUB}} &= M_{HUB}\,R_U\,g\,(\cos\chi\sin Q_3\cos q_4)\\
F^*_{3_{HUB}} &= -\ddot{q}_3\left[M_{HUB}\,R_U + I_{HUB}\right] - M_{HUB}\,R_U\,\dot{q}_4^2\sin q_3\cos q_3\\
F^*_{4_{HUB}} &= -\ddot{q}_4\left[M_{HUB}\,R_U\sin^2 q_3\right] - M_{HUB}\,R_U\,\dot{q}_3\dot{q}_4\sin q_3\cos q_3
\end{aligned} \tag{2.5.1}$$

The generalized active and inertia forces are combined using Eq. (2.5.1) into the form of Eq. (2.5.10) for numerical solution.

2.6 Generator Model

Two variable-speed generator models are to be used for the generator restraining torque. The first model is for an induction generator that has small variations about a rated rotation speed due to generator slip. The second model is for a variable-speed generator operating at a constant tip-speed ratio.

For an induction generator the restraining torque can be divided into two components:

$$T = T_{electrical} + T_{losses} \tag{2.6.1}$$

where,

$$T_{electrical} = \frac{c_e N^2}{\eta_{GB}} (\Omega - \Omega_0)$$

$$T_{losses} = \frac{N}{\eta_{GB}} \left(T_{fixed} \left(\frac{\Omega}{\Omega_0} \right) + T_{variable} \left(\frac{\Omega - \Omega_0}{\Omega_R - \Omega_0} \right)^2 \right) \quad (2.6.2)$$

where N is the gearbox step-up ratio, η_{GB} is the gearbox efficiency, and c_e, Ω_0, and Ω_R are constants. The fixed and variable losses are functions of the generator fixed-loss factor f and can be expressed as:

$$T_{fixed} = f \left(\frac{1}{\eta_{GEN}} - 1 \right) \frac{P_{Rated}}{\Omega_R}$$

$$T_{variable} = (1 - f) \left(\frac{1}{\eta_{GEN}} - 1 \right) \frac{P_{Rated}}{\Omega_R} \quad (2.6.3)$$

where η_{GEN} is the generator maximum efficiency and P_{Rated} is the generator rated power output.

The variable-speed generator operating at constant tip-speed ratio should have a restraining torque that varies to allow the rotor speed to follow the wind speed preserving the tip speed ratio, $R\Omega/V$. In most wind turbine applications, future wind speed measurements are not available. The variable speed controller has only past torque and wind histories to use in its control algorithm. This can result in the generator lagging the wind, reducing the power captured. The following relation for the generator torque follows the optimum power coefficient as a function of the tip-speed ratio, λ. The tip-speed ratio is based on a moving average of the last 100 wind speed values. This results in slowly varying generator torque:

$$T = \frac{\frac{1}{2} \pi \rho V^2 R^3 C_p}{\lambda} \quad (2.6.4)$$

The variable-speed generator can also be used as a start-up motor or a shut-down brake. For a motor the generator torque has a negative sign. The generator braking torque must be greater than the aerodynamic torque for deceleration of the rotor. Both the motor and brake can be a function of time, rotor speed, or any other generator variable.

2.7 Deterministic Wind Model

The deterministic wind model consists of two parts: wind shear and tower shadow. The shear model uses a power law expression to determine the velocity distribution with height:

$$V = v_{HUB}\left(1 - \frac{r \sin q_4}{H_{HUB}}\right)^n \tag{2.7.1}$$

where q_4 is the azimuth angle, which starts when the blade is parallel to the ground. The blade starts moving downward; therefore, a negative sign is used in Eq. (2.7.1). H_{HUB} is the hub height, r is the blade radius location, and n is the power law exponent.

The tower shadow occurs when the blade is straight down and in the wake from the upstream tower. The shadow model assumes the tower wake to have a cosine-squared-shaped deficit where the blade passes through it. Assuming a wake width of two diameters, an expression for the velocity distribution can be found using a momentum balance:

$$V(y) = V_\infty\left(1 - \epsilon \cos^2\left(\frac{\pi\, y}{2\, D}\right)\right) \tag{2.7.2}$$

where the velocity deficit can be expressed as a function of the tower drag coefficient:

$$\epsilon = \left(\frac{2}{3}\right)\left[1 - \left(1 - \frac{3\, C_D}{2}\right)^{\frac{1}{2}}\right] \tag{2.7.3}$$

In the case of the ESI-80, the tower has three legs in a truss arrangement. The tower diameter d in Eq. (2.7.2) can be expressed as the distance between two legs, and the tower drag coefficient C_D is the sum of the individual tower leg drag coefficients.

2.8 Numerical Solution Technique

A numerical solution of the four equations of motion is achieved using a fourth-order Adams-Bashforth Predictor formula together with an Adams-Moulton Corrector formula. This numerical method is not self starting; therefore, a fourth-order Runge-Kutta method is employed to calculate the first three points.

2.9 Code Organization

The computer code based on the previous theoretical development was named the DRT code. A detailed description of the procedure to operate this code can be found in the DRT users guide [42].

The DRT code is written in standard FORTRAN 77. The code operates in the time domain using time as the marching variable. Figure 2.5 shows a flowchart of the different subroutines used. Subroutine INPUT reads in the input file containing the characteristics of the turbine to be modeled. Subroutine INTERP takes the blade data and interpolates them at a constant blade increment. This increment is the integration increment used for calculation of the generalized active and inertia forces. Subroutine COEF determines the number of values that are used repeatedly throughout the program and calculates the blade mode shapes. The main program starts here at time equal to zero. The total time the code will run depends on the option chosen. The teeter and variable-speed degrees of freedom can be either start-up, shut-down, or normal operation with two different generator models. Subroutine SOLVER solves the four equations of motion using the numerical scheme described in section 2.8. Subroutine RTHS (right-hand side) calculates the generalized and inertial forces and integrates them down both blades. RTHS calls subroutines TRAN, CALC, GENTORQ, and GAUSS. Subroutine TRANS calculates the coordinate transformations given in Eq. (2.3.12). Subroutine CALC determines the aerodynamic normal and tangential forces, Eq. (2.4.15), based on the method in section 2.4. Subroutine CALC calls subroutine WIND, which calculates the wind shear and tower shadow contributions described in section 2.7. Subroutine CALC calls subroutine AERO, which has the lift and drag airfoil characteristics as a function of angle of attack and airfoil thickness. Subroutine GENTORQ supplies the generator restraining torque based on a model from section 2.6. Subroutine GAUSS inverts the matrix Eq. (2.5.10) for solution in subroutine SOLVER. If turbulence is desired, the turbulent wind values are read by subroutine RTHS for every time increment. The main program checks after every new set of values are calculated to see if it should be writing loads to the output file and to see if it has completed the run. The various loads, blade bending moments, rotor thrust, rotor torque, and the generator output power are calculated in subroutine RTHS.

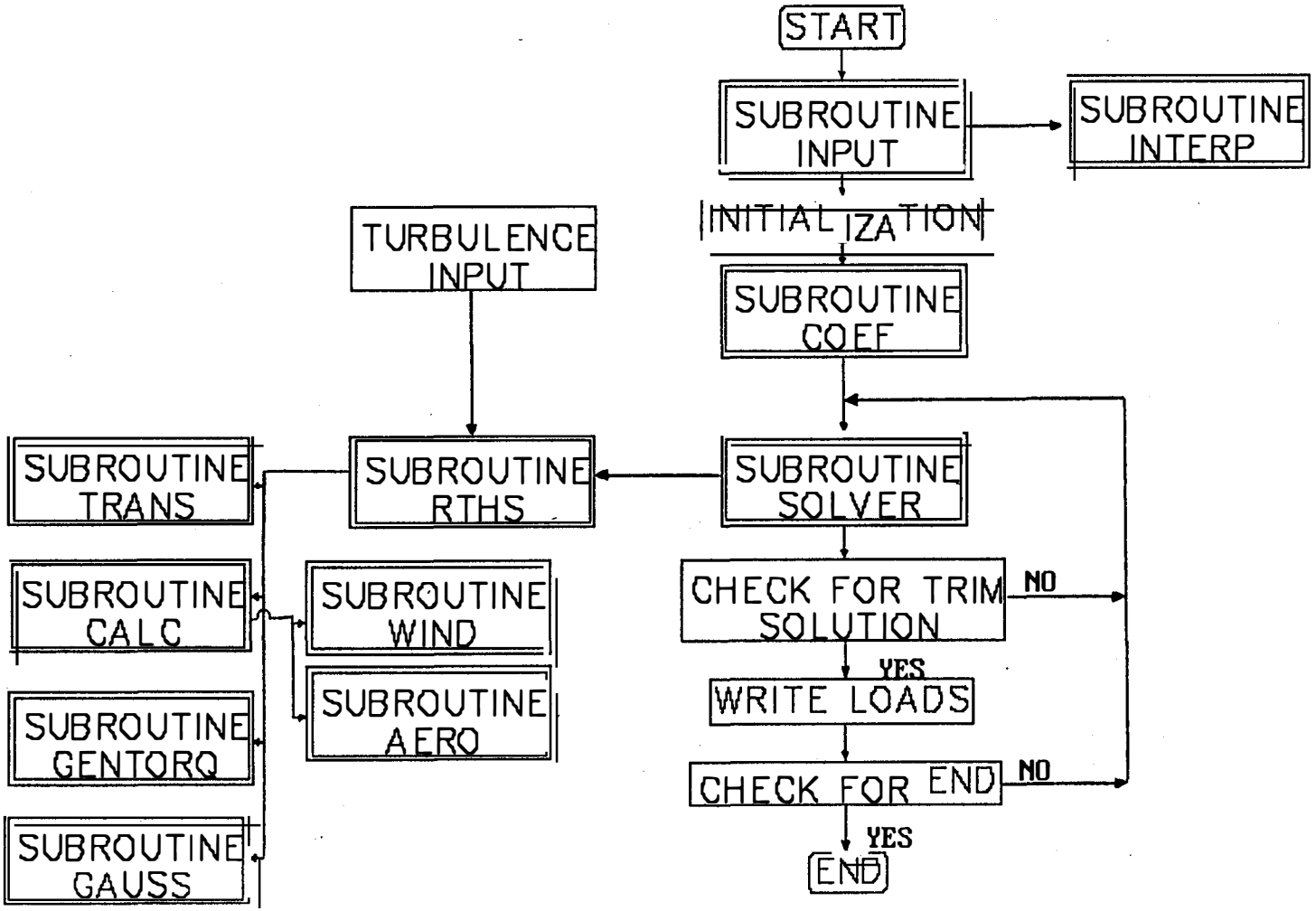

Figure 2.5. Code Flowchart.

3. MODEL VALIDATION

The model was validated using two methods. The results from the model were compared to results from simple models where analytical solutions could be found. Additionally, comparisons between model load predictions and experimental loads were also made. The experimental loads were taken from an ESI-80 wind turbine, which is documented in the DRT user's guide [42]. Loads that were compared were blade root bending moments, rotor torque, and rotor thrust for both mean and cyclic loads.

3.1 Simple Beam

In order to validate the static deflections and natural frequencies of the rotor blades, a simple beam, together with linear aerodynamics, was implemented in the code. The blade properties of chord, twist, mass, and stiffness were assumed to be constant over the length of the blade. Undersling, delta-3, the elastic bending axis rotation, and coning were set at zero, and the variable speed and teeter degrees of freedom were turned off. Lift was assumed to vary linearly with the angle of attack, $C_L = 2\pi\sin\alpha$. The induced velocity was assumed to be constant over the blade given by the relation for the induction factor as:

$$a = \frac{c\,\Omega}{2\,V_\infty} \tag{3.1.1}$$

Ignoring the cyclic effect of gravity, a relation for the static tip deflection can be written as:

$$q_{static} = \frac{\int_0^R f_n\,\phi\,dr}{\left(\int_0^R \left(\frac{\partial^2\phi}{\partial\bar{r}^2}\right)^2 EI\,d\bar{r} + \int_0^R T\left(\frac{\partial\phi}{\partial\bar{r}}\right)^2 d\bar{r}\right)} \tag{3.1.2}$$

where,

$$T = \int_R^r \Omega^2 \mu \bar{r} \, d\bar{r} \tag{3.1.3}$$

and,

$$f_n = \frac{1}{2} \rho W^2 c C_L \cos \phi_\alpha \tag{3.1.4}$$

which can be written as:

$$f_n = \rho \pi c r \Omega V \left(1 - \frac{C \Omega}{2 V}\right) \tag{3.1.5}$$

The numerator of Eq. (3.1.2) can be expressed as:

$$\rho \pi C \Omega V \left(1 - \frac{C \Omega}{2 V}\right) \int_0^R r \phi_1 \, dr \tag{3.1.6}$$

Letting the shape function be that from Eq. (2.2.9), with a value of b=0, ρ=1 kg/m^3, c=.25 m, Ω=60 rpm, V=10 m/s, R=10 m, EI=5,000,000 N-m^2, and μ=10 kg/m, gives a static deflection of 0.07747 meters. Implementing the linear lift and the induction factor given in Eq. (3.1.1), the code gives a static deflection within a half of a percentage point of the analytical value when the integration step size is one-hundredth of the blade length.

Using the same conditions, a relation for the blade flapping natural frequency can be written as:

$$w_n^2 = \frac{\int_0^R EI \left(\frac{\partial^2 \phi}{\partial r^2}\right)^2 dr + \int_0^R \left(\int_R^r \Omega^2 \mu \bar{r} d\bar{r}\right) \left(\frac{\partial \phi}{\partial r}\right)^2 dr}{\int_0^R \mu \phi^2 \, dr} \tag{3.1.7}$$

This gives a value for the natural frequency of 4.165 Hertz. The code predicted a value within a half of a percentage point, when the integration step size was set at one hundredth of the blade length.

3.2 Linearized Teeter Motion with Delta-3

A analytical expression can be obtained for the teeter motion through simplification and linearization of the teeter equation (r=3 in section 2.6). The analytical expression can be used for validation of

the teeter motion in the code. Letting the blade displacements and motions be zero, setting the rotor speed constant, and ignoring higher order terms, the teeter equation can be written as:

$$\sum_{j=1}^{2} \int_0^R (f_n r\cos\delta_3 - \mu g \sin q_3 \sin q_4 r\cos\delta_3)\, dr - \sum_{j=1}^{2} \int_0^R \mu \left(\ddot{q}_3(\cos\delta_3\, r)^2 + \Omega^2 \sin q_3 \cos q_3 (\cos\delta_3\, r)^2\right) dr = 0 \tag{3.2.1}$$

where coning, the elastic bending axis rotation, and the undersling have been set to zero. Linearizing the teeter angle q_3 and assuming the two blade mass distributions are the same, Eq. (3.2.1) can be written as:

$$\ddot{q}_3\, I \cos^2\delta_3 + q_3\, I\, \Omega^2 \cos^2\delta_3 = \int_0^R f_n\, r\, \cos\delta_3\, dr\Big|_{\text{blade 1}} - \int_0^R f_n\, r\, \cos\delta_3\, dr\Big|_{\text{blade 2}} \tag{3.2.2}$$

Assuming linear lift, an induced velocity as given in Eq. (3.1.1) and a linear wind shear Eq. (3.1.4) can be written as:

$$f_n = \rho\, \pi\, c\, r\, \Omega\, (V(1-a)) \pm (\Omega \sin\delta_3\, q_3 + \dot{q}_3 \cos\delta_3)\, r \tag{3.2.3}$$

$$(-\text{ blade 1}) \qquad (+\text{ blade 2})$$

Combining Eqs. (3.2.2) and (3.2.3) and integrating along the blade gives:

$$\ddot{q}_3 + B\cos\delta_3\, \Omega\, \dot{q}_3 + (B\sin\delta_3 + 1)\, \Omega^2\, q_3 = \frac{B\,\Omega}{2\,R} (V_{top} - V_{bottom}) \sin(\Omega t + \delta_3) \tag{3.2.4}$$

where,

$$B = \frac{\rho\, \pi\, R^4\, c\, \Omega}{2\, I \cos^2\delta_3} \tag{3.2.5}$$

with a change of variables:

$$\frac{d(\ )}{dt} = \frac{d(\ )}{dq_4}\frac{dq_4}{dt} = \Omega \frac{d(\ )}{dq_4} \tag{3.2.6}$$

Eq. (3.2.4) can be written as:

$$q_3'' + B\cos\delta_3\, q_3' + (B\sin\delta_3 + 1)q_3 = \frac{-B\,(V_{top} - V_{hub})}{R\,\Omega}\sin(q_4 + \delta_3) \tag{3.2.7}$$

Looking for a steady-state solution of the form:

$$q_3 = C_1 \sin q_4 + C_2 \cos q_4 \tag{3.2.8}$$

results in the analytical solution:

$$q_3 = \frac{V_{top} - V_{hub}}{R\,\Omega}\cos(q_4 + 2\delta_3) \tag{3.2.9}$$

Using the same parameters as in section 3.1 and implementing the linear lift, the induction factor from Eq. (3.1.1), and a difference of 2 meters per second for (V_{top} - V_{hub}), the analytical solution is compared to the code prediction for three values of delta-3 in Figure 3.1. The code accurately predicts the analytical solution for all three cases. Note that the relation for the teeter angle in Eq. (3.2.9) is independent of blade mass and inertia.

3.3 Mean Loads

The ESI-80 was used for comparisons of mean loads. The data for both the mean and cyclic loads were digitized from the report by Musial et al. [46]. The measured mean loads were determined by averaging the values in 1-mile-per-hour divisions. Data was taken at 5 Hertz from 15 to 30 minutes. Some data were taken on different days when the atmospheric conditions were different. This can be seen on Figure 3.2, which shows a staircase effect on the bending moment. Atmospheric conditions were not reported. The code was run using only the teeter option. The variable speed and turbulence options were not used.

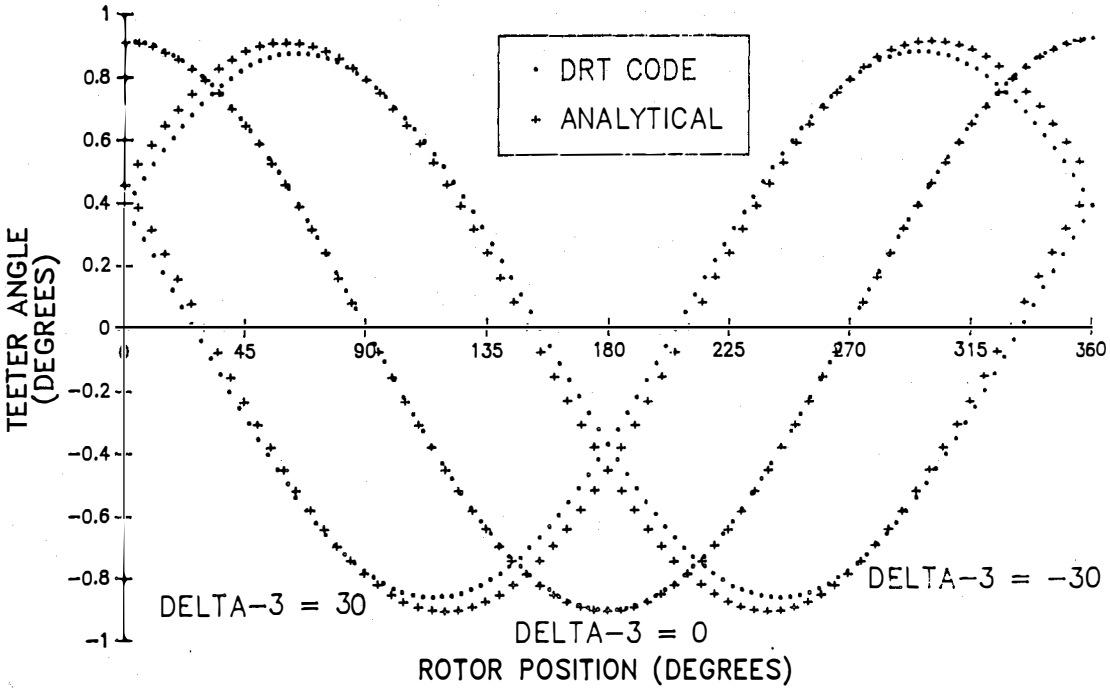

Figure 3.1. Comparison of Analytical and Code Teeter Angle

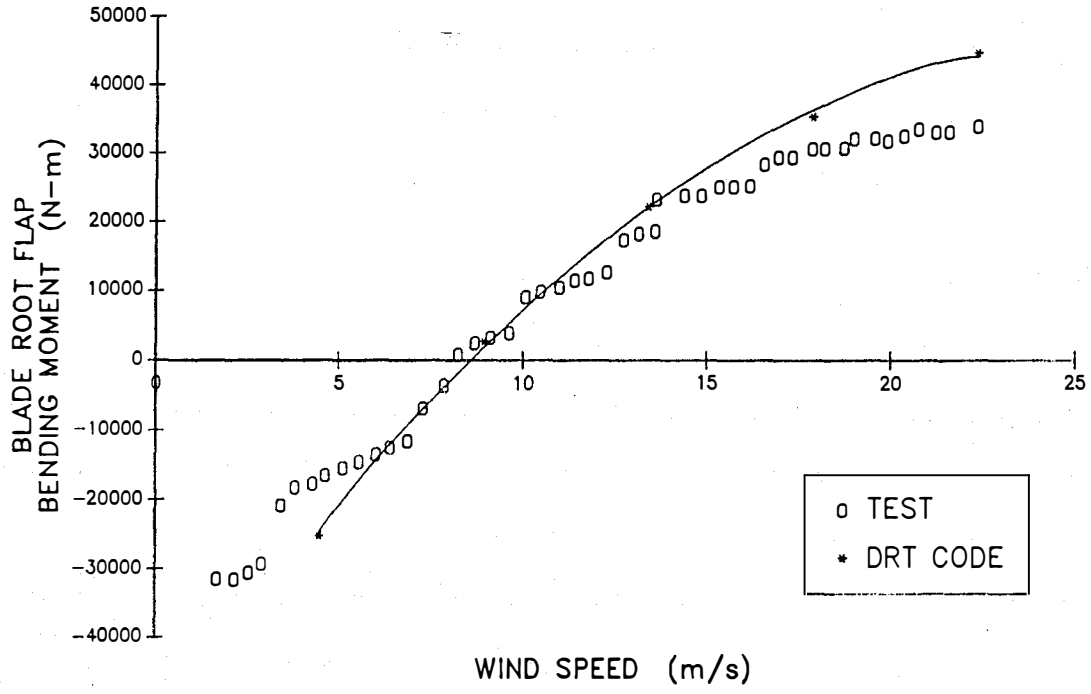

Figure 3.2. Comparison of Mean Root Flap Bending Moments

Figure 3.2 compares code predictions to test root bending moments. The code predictions match well within the standard deviation for the data, which is approximately 5000 N-m, except in the high-wind-speed portion where the prediction is conservative. The mean root bending moment is the difference between two large moments, the aerodynamic moment, and the centrifugal moment. In the high-wind-speed case, where aerodynamic stall characteristics are not well known, a small error in either of these would be greatly exaggerated in their difference. Figure 3.3 shows the comparison of rotor thrust, and Figure 3.4 compares rotor torque. The code predictions for both of these loads matches the data well.

3.4 Cyclic Loads

The cyclic data used for comparison were recorded at 24 Hertz for 5- to 20-minute intervals and then averaged versus rotor position. This coarse data sampling rate combined with a rotor averaging increment of 15 degrees results in a fair amount of uncertainty with the cyclic data. The code was run using the teeter option. The variable-speed and turbulence options were not used.

Figure 3.5 compares the teeter angle at 42 miles per hour. The code was run with a 3.6 degree interval. The prediction lags the data by approximately 30 degrees and underpredicts the amplitude. The ESI-80 has teeter dampers when teeter amplitudes of 2 degrees are reached, but that is not a concern for this case as neither the data nor the predictions exceed that value. Figure 3.6 compares the root bending moment at 22 miles per hour. The prediction follows the general trend of the data; however, the prediction shows more detail in the blade flapping response, especially in the tower shadow region where the blade passes through the wind deficit and then springs out of it. This occurs at a rotor position of approximately 90 degrees. The blade natural frequency of 2.5 Hertz also can be seen in this figure. Figure 3.7 shows the comparison of cyclic rotor thrust. The effect of the blade entering the tower shadow can be seen at 90 degrees for blade one and 270 degrees for blade two. The prediction appears to have a phase lag of 90 degrees. Thrust measurements were taken at the base of the tower, so it is possible that tower motion caused this anomaly. Figure 3.8 shows cyclic rotor torque. The prediction shows the same trend with exaggerated tower shadow effects. The larger

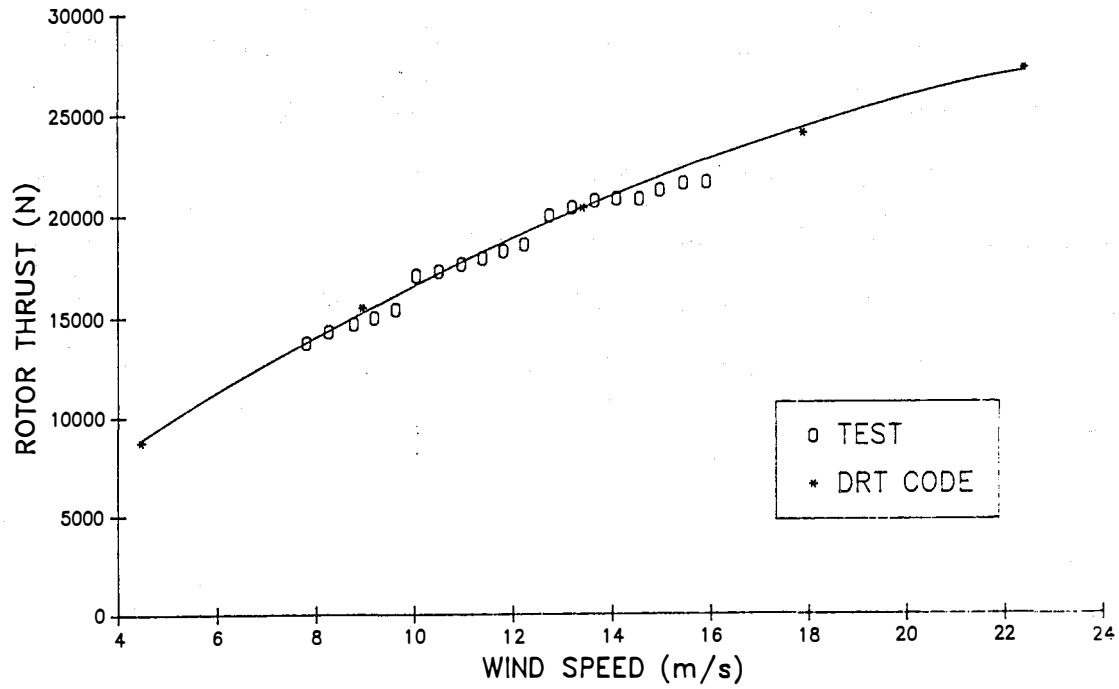

Figure 3.3. Comparison of Mean Rotor Thrusts.

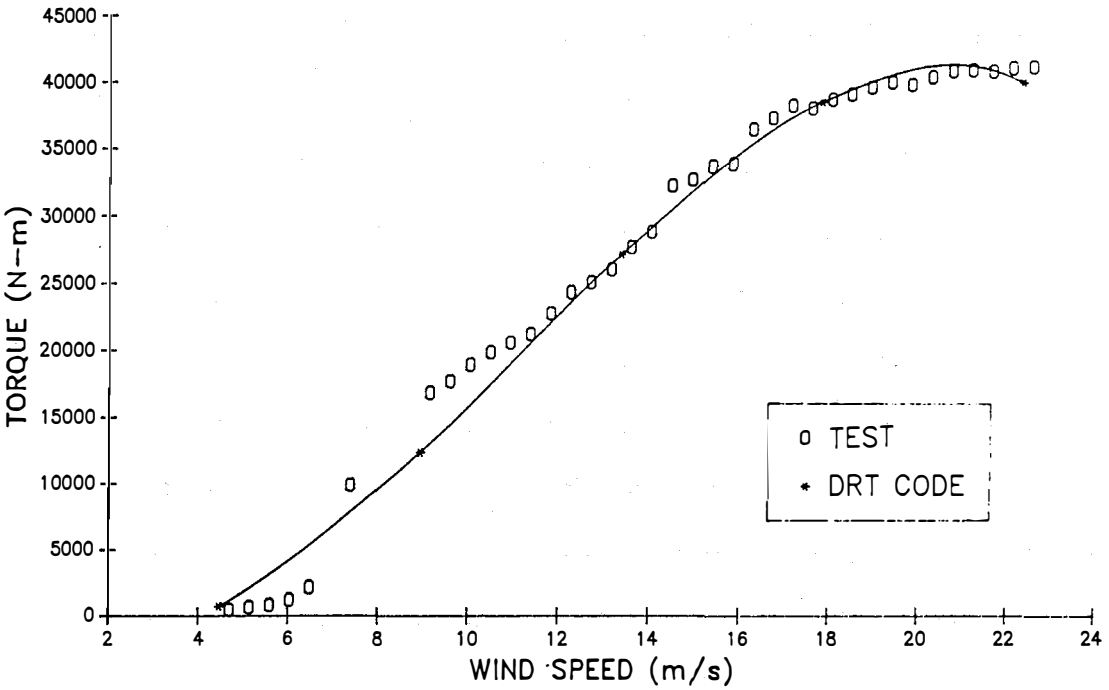

Figure 3.4. Comparison of Mean Rotor Torques.

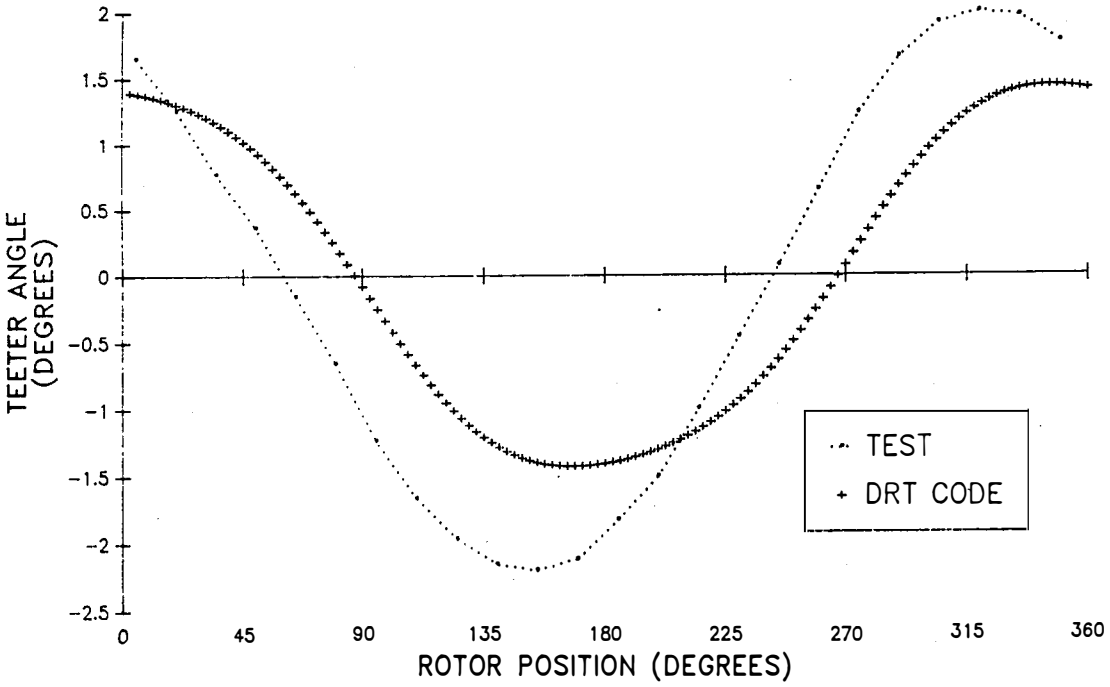

Figure 3.5. Comparison of Teeter Angle Comparison at 42 mph.

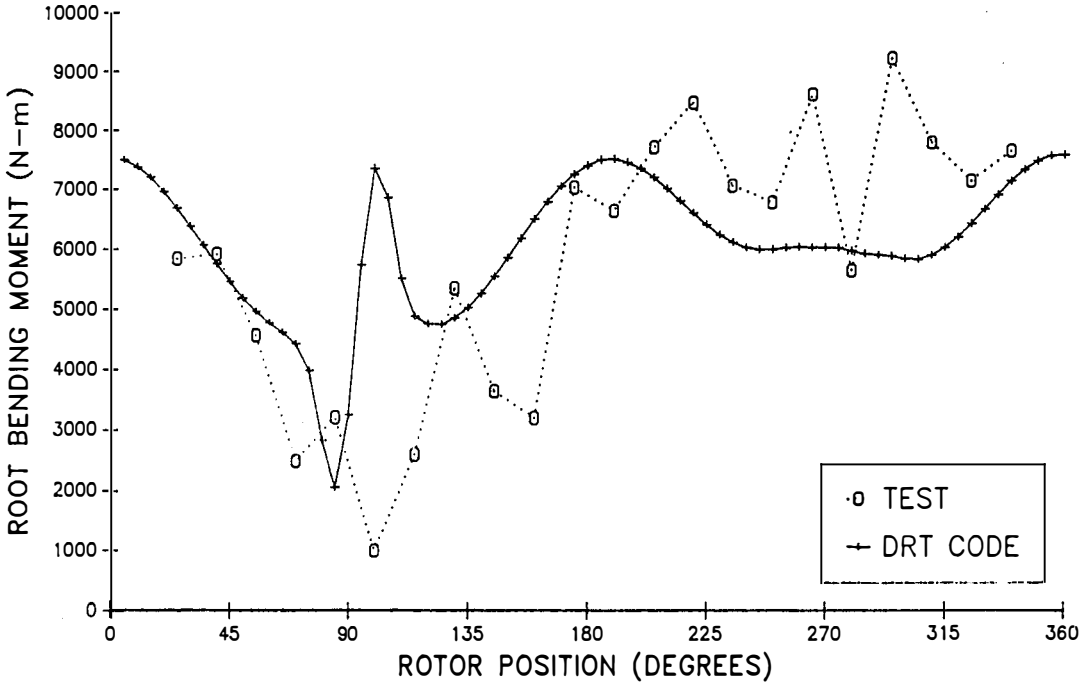

Figure 3.6. Comparison of Cyclic Root Flap Bending Moment at 22 mph.

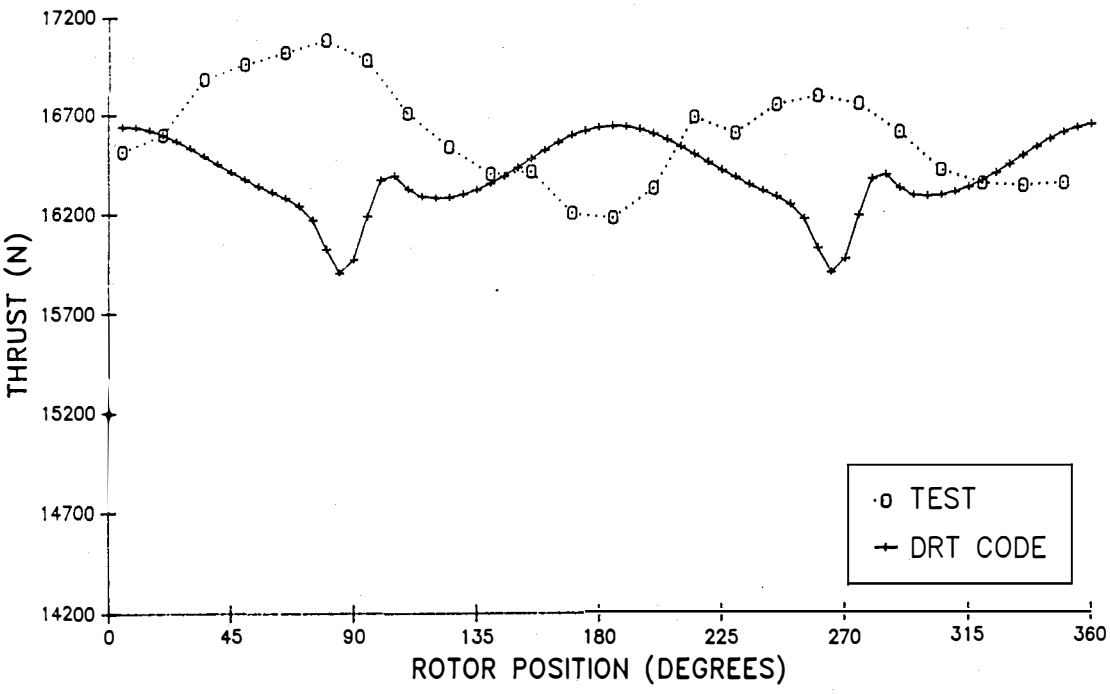

Figure 3.7. Comparison of Cyclic Rotor Thrust at 22 mph.

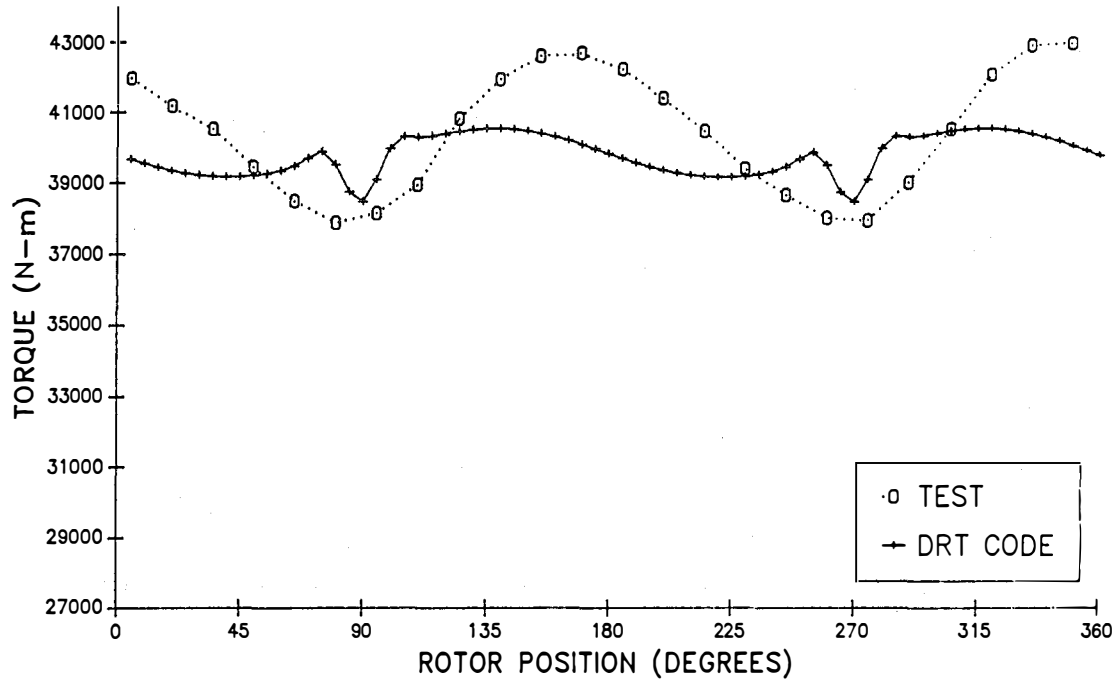

Figure 3.8. Comparison of Cyclic Rotor Torque at 44 mph.

amplitude for both the thrust and torque data suggests a yaw error. The yaw errors were unreported for these cases.

3.5 Turbulence-Induced Loads

Turbulence simulation for HAWT analysis codes that model only one blade on a rigid hub with a constant rotor rotation speed is well documented [37]. The turbulence simulation required by this code is complicated by the teeter mechanism and the variable-speed rotor. Coherent turbulence is needed on both blades because of blade interaction through the teeter motion. A variable-speed rotor requires simulation that does not depend on a constant rotor speed. The only turbulence model that meets these criteria is the code developed by Veers [36].

The Veers code was used to generate turbulence values for the following comparisons. Full-field turbulence was created for 72 rotor positions at one radial location for 1024 points. The single radial location turbulence value was used for the entire blade in the analysis code. The 80% radius was chosen because this location more accurately predicts multiradial station turbulence; this was shown by Weber [47]. Two wind cases were used for comparison, these were 22 miles per hour and 40 miles per hour. Both had a turbulence intensity of 15% and a coherence decrement of 12. Three cases were run for each wind speed. The code was run using constant rotor speed with and without the teeter degree of freedom and with the induction generator model with teeter. Constant rotor speed corresponds to a synchronous generator.

Figure 3.9 shows the power spectral density (psd) of the root bending moment as a function of frequency in Hertz for the synchronous generator cases with and with out teeter. The teeter case shows much less energy at 1 Hertz, which is the one-per-revolution component. This is expected because the teeter motion responds to the one-per-revolution bending moment component. Only minor differences are noted for the rest of the spectrum. Figure 3.10 compares the psd's of the synchronous and induction models with teeter. The induction model has less energy below 1 Hertz and a slight increase above relative to the synchronous model psd. The induction model has a mean rotor speed that is about 1% higher than the constant rotor speed. This is seen in the one period peak slightly above

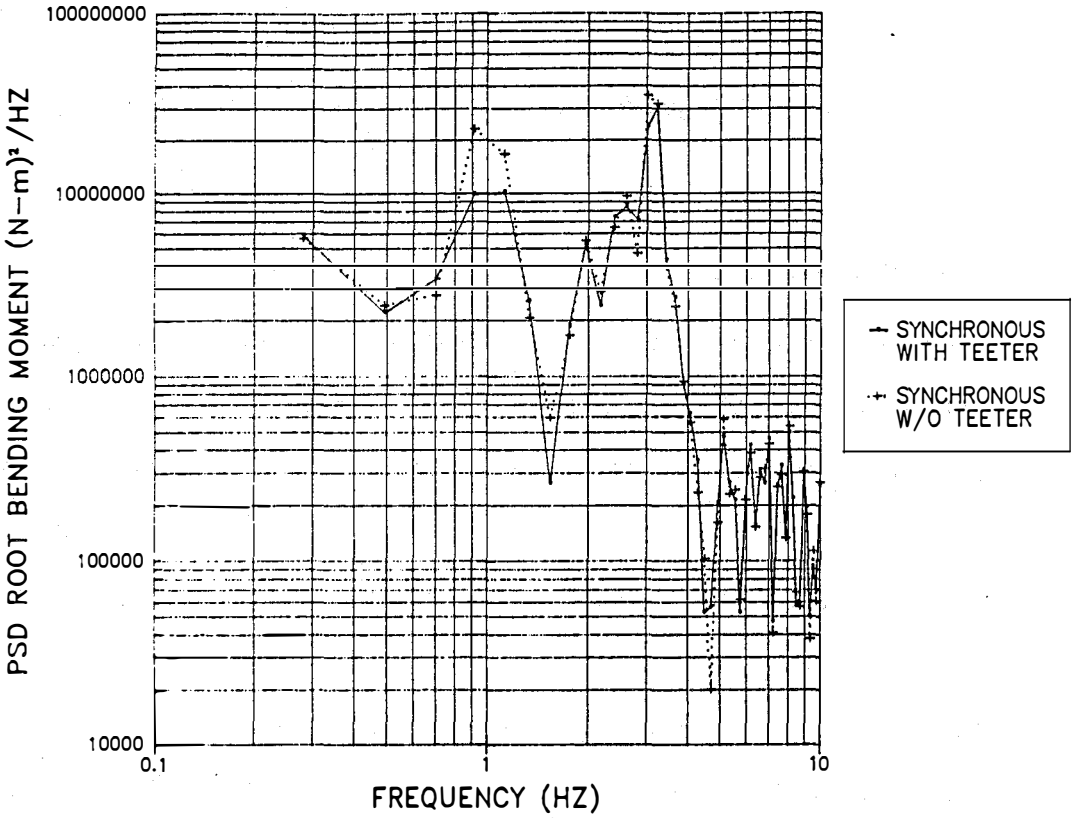

Figure 3.9. Comparison of Power Spectral Densities of Blade Root Flap Bending Using a Synchronous Generator with and without Teeter at 40 mph.

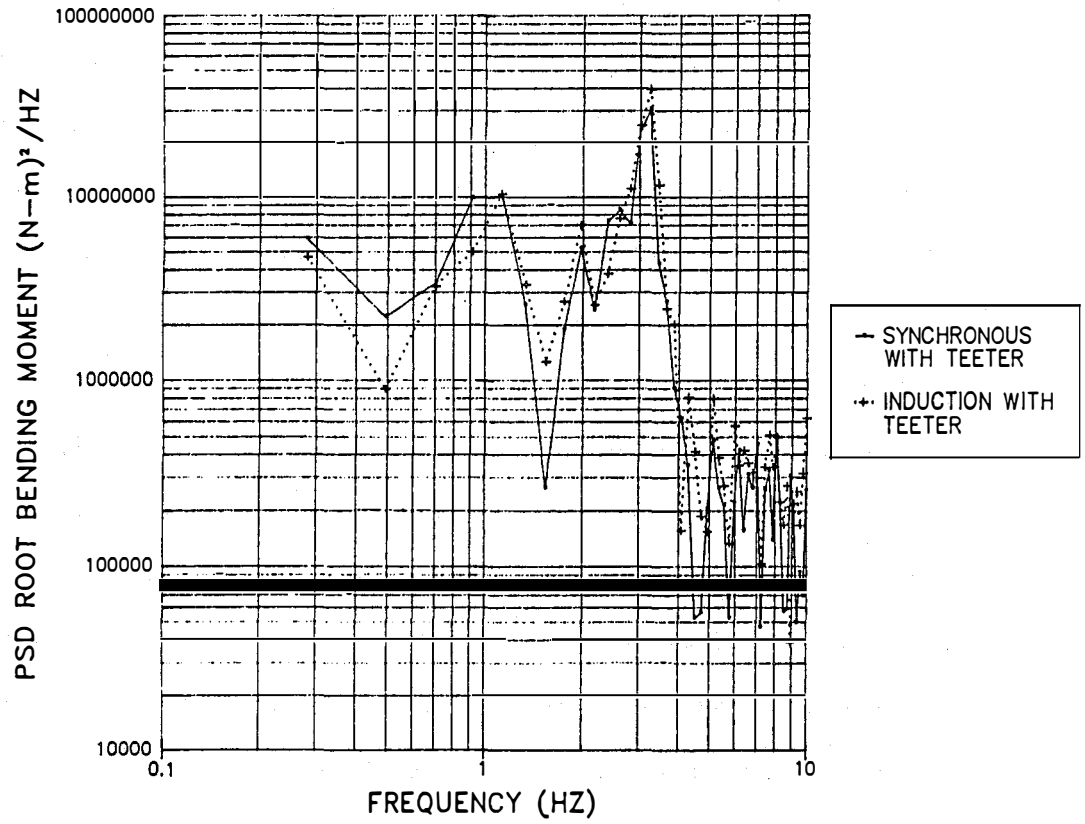

Figure 3.10. Comparison of Power Spectral Densities of Blade Root Flap Bending for Synchronous and Induction Generator with Teeter at 40 mph.

1 Hertz. The average rotor speed increase also shifts the higher harmonics. The blade natural frequency at approximately 2.5 Hertz can be seen in both figures. The three-per-revolution harmonic has more energy for all three cases due to its proximity to the blade natural frequency. The mean values for root flap bending moment differed little, except for a slight increase with the induction model due to increased rotor speed. The standard deviations were also comparable. Figures 3.11 and 3.12 show the same cases as Figures 3.9 and 3.10, respectively, for the 22 mile-per-hour wind speed. The same trends are seen as in the 40 mile-per-hour wind speed case. The code prediction for the root flap bending moment with the induction generator model was azimuth averaged and compared to the same data used in Figure 3.6. This comparison can be seen in Figure 3.13. The blade response to the tower shadow is no longer as prevalent as previous comparisons, and the predictions show the same choppiness as the data due to azimuth averaging.

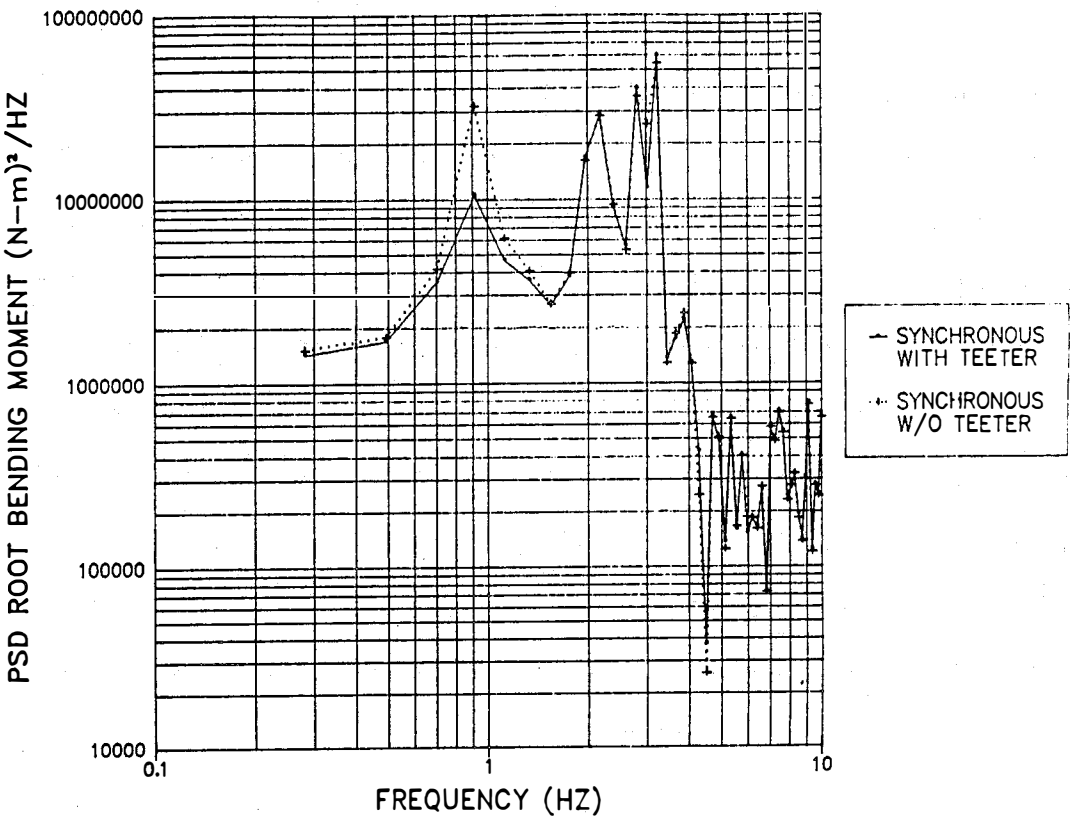

Figure 3.11. Comparison of Power Spectral Densities of Blade Root Flap Bending Moment for a Synchronous Generator with and without Teeter at 22 mph.

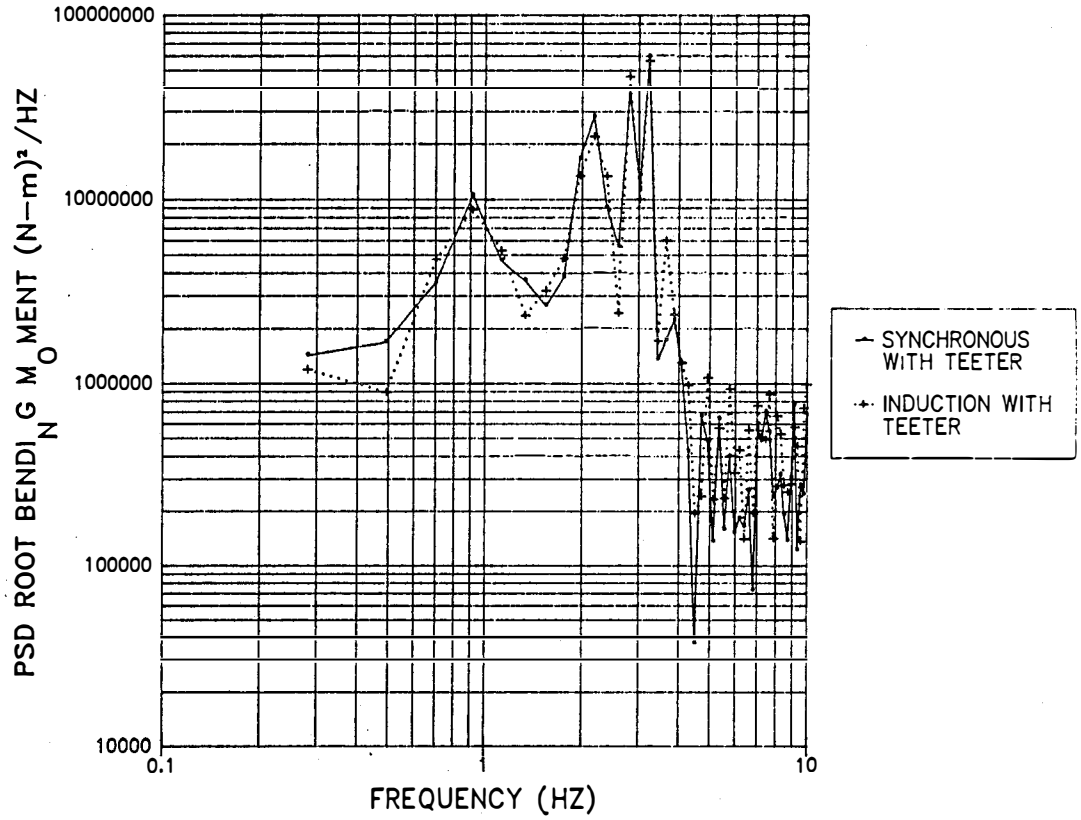

Figure 3.12. Comparison of Power Spectral Densities of Blade Root Flap Bending Moment for a Synchronous and Induction Generator with Teeter at 22 mph.

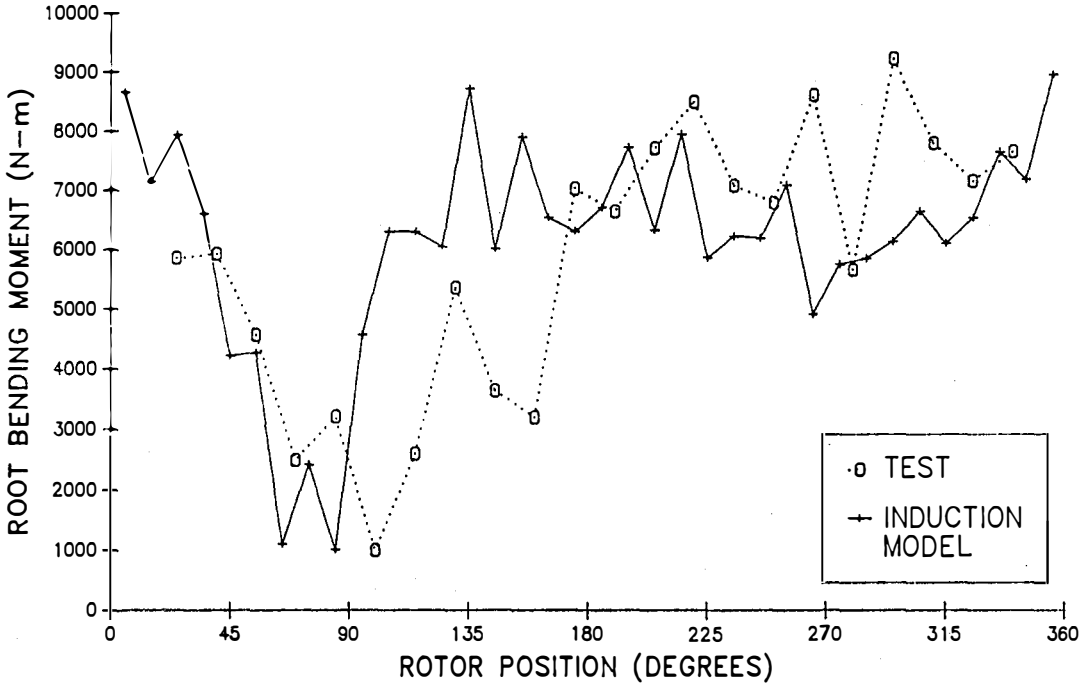

Figure 3.13. Comparison of Cyclic Root Flap Bending Moment at 22 mph with Induction Generator Model.

4. CLOSURE

A four-degree-of-freedom time-domain computer model of a two-bladed, teetered HAWT with a variable-speed rotor has been developed and validated. Generator models for synchronous, induction, and variable-speed machines can be implemented in the code. Aerodynamic loading consists of deterministic effects and stochastic effects.

4.1 Development

The two turbine blades were modeled as flexible cantilevered beams, which are allowed to teeter about the low-speed shaft. The low-speed shaft is connected to a generator through a gearbox. Provisions are made for delta-3, twist, precone, undersling, tilt, yaw, and an angle between the elastic bending axis and the rotor plane. The aerodynamic loads are determined using axial momentum theory together with deterministic wind effects including wind shear, tower shadow, and stochastic wind effects from atmospheric turbulence. The equations of motion are solved using a predictor-corrector solving scheme.

4.2 Validation

Predictions from the model were compared to simple models with analytical solutions and to experimental loads. The following conclusions were reached:

1. The model duplicates the flapwise static-tip deflection and blade natural frequency of a simple beam model.
2. The model duplicates the teeter motion of a simple linearized teeter model for a range of delta-3 values.
3. The model determines the mean bending moment, thrust, and torque loads for the ESI-80 well within acceptable error limits.
4. The model predicts the general trends of cyclic teeter angle, flap bending moment, torque, and thrust for the ESI-80. The cyclic ESI-80 data have a large uncertainty due to a coarse sampling rate.

5. A full-field turbulence model was implemented to test the synchronous and variable-speed induction generator models.

4.3 Future Work

Future work consists of using the model as a tool for a variety of studies. These studies include:

1. Parametric analysis of the effect of undersling, delta-3, the elastic bending axis rotation, and blade mass and twist differences.
2. Start-up and shut-down schemes utilizing the variable-speed degree of freedom. Sequences include motorized or freewheeling startups and mechanical brake or blade feathering shutdowns.
3. Control algorithms for variable-speed models can be assessed using the variable-speed degree of freedom.

A provision for elastic blade flapping to be perpendicular to each blade element's minimum moment of inertia, instead of the current flapping motion that is perpendicular to the entire blade's minimum moment of inertia, exists in the code. This will cause blade motion to have more effect in the torsional rotor loads.

Another drive-train degree of freedom can be added to the model. The effect of gearbox and drive-train stiffness and damping on both rotor and generator loads can be examined. These effects are important when impact torques due to starting and stopping are applied. Variable-speed generator models that reduce drive-train resonances could also be explored.

5. REFERENCES

1. Wilson, R.E., Walker, S.N., Weber, T.L., Hartin, J.R., "A Comparison of Mean Loads and Performance Predictions with Experimental Measurements for Horizontal Axis Wind Turbines," Eighth ASME Wind Energy Symposium, Houston, Texas, Jan. 22-29, 1989.

2. Wright, A.D., Buhl, M.L., Thresher, R.W., "FLAP Code Development and Validation," SERI/TR-217-3125, January 1988.

3. Hansen, A.C., Butterfield, C.P., Cui, X., "Yaw Loads and Motions of a Horizontal Axis Wind Turbine," European Wind Energy Conference (EWEC), Glasgow, Scotland, July 10-13, 1989.

4. Hartin, J.R., "Evaluation of Prediction Methodology for Blade Loads on a Horizontal Axis Wind Turbine," Ninth ASME Wind Energy Conference, New Orleans, Louisiana, January 14-18, 1990.

5. Morgan, C.A., Garrad, A.D., Hassan, U., "Measured and Predicted Wind Turbine Loading and Fatigue," EWEC, Glasgow, Scotland, July 10-13, 1989.

6. Derdelinckx, R., Hirsh, Ch., "Dynamic Load Calculations of Horizontal Axis Wind Turbines," EWEC, Glasgow, Scotland, July 10-13, 1989.

7. McNerny, G., "The Effect of Variable Speed Operation on the Cost Projections for Advanced Wind Turbines," Ninth ASME Wind Energy Symposium, New Orleans, Louisiana, January 14-18, 1990.

8. Hock, S.M., Thresher, R.W., Cohen, J.M., "Performance and Cost Projections for Advanced Wind Turbines," Ninth ASME Wind Energy Symposium, New Orleans, Louisiana, January 14-18, 1990.

9. Husse, G., Perpeintner, R., "The Effect of Variable Rotor Speed on the Design and Operation of a WEC," EWEC, Hamberg, West Germany, Oct. 22-26, 1984.

10. Anderson, T.S., Hughes, P.S., Klein, F.F., Mutone, G.A., "Double-Fed Variable Speed Generating System Testing," Fourth ASME Wind Energy Symposium, Dallas, Texas, February 17-21, 1985.

11. Nordquist, P., "Investigation of Electrical Power Pulsations from a 2 megaWatt Wind Turbine Generator," EWEC, Glasgow, Scotland, July 10-13, 1989.

12. Ernst, J., "Control of a Variable Speed WEC with a Synchronous Generator and a DC Link Convertor," EWEC, Hamburg, West Germany, Oct. 22-26, 1984.

13. Bongers, P., Engelen, T., Dijkstra, S. Kock, Z., "Optimal Control of a Wind Turbine in Full Load," EWEC, Glasgow, Scotland, July 10-13, 1989.

14. Schmidt, W.C., Birchenough, A.G., "Evaluating Variable Speed Generating Systems on the DOE/NASA MOD-0A Wind Turbine," Wind Power, San Francisco, California, August 27-30, 1985.

15. Carlson, O., Tsiolis, S., Johansson, G., "Variable Speed AC-Drive System with Pitch or Yaw Control," Wind Power, San Francisco, California, October 5-8, 1987.

16. Matsuzaka, T., Tsuchiya, K., Yamada, S., Kitahara, H., "A Variable Speed Wind Generating System and Its Test Results," EWEC, Glasgow, Scotland, July 10-13, 1989.

17. Husse, G., Einmann, R., "Wind Power Plant WKA-60 for Helgaland - Status of the Project," EWEC, Glasgow, Scotland, July 10-13, 1989.

18. Coriante, D., Foli, U., Sesto, E., Taschini, A., Aviola, S., Zappala, F., "GAMMA 60 1.5 MW WTG," EWEC, Glasgow, Scotland, July 10-13, 1989.

19. Johnson, W., *Helicopter Theory*, Princeton University Press, 1983.

20. Bramwell, A.R.S., *Helicopter Dynamics*, Edward Arnold Ltd., London, 1976.

21. Gessow, A., Meyers, G.C., *Aerodynamics of the Helicopter*, Fredrick Ungar Publishing Co., New York, 1952.

22. Hodges, D.H., "Review of Composite Rotor Blade Modeling," *AIAA J.* Vol. 28, No. 3, 1990.

23. Ormiston, R.A., Peters, D.A., "Hingeless Helicopter Rotor Response with Non-Uniform Inflow and Elastic Bending," *J. Aircraft*, Vol. 9, No. 10, 1972.

24. Miller, R.H., "Methods for Rotor Aerodynamic and Dynamic Analysis," *Prog. Aero. Sci.*, Vol. 22, 1985.

25. Piziali, R.A., "Method for Solution of the Aeroelastic Response Problem for Rotating Wings," *J. Sound Vib.*, Vol. 4, No. 3, 1966.

26. Kottapalli, S.B.R., Friedman, P.P., "Coupled Rotor/Tower Aeroelastic Analysis of HAWT Blades," *AIAA J.*, Vol. 18, No. 9, 1980.

27. Feitso, E.A.N., Mead, D.J., "Parametric Resonance in HAWTS," EWEC, Glasgow, Scotland, July 10-13, 1989.

28. Weyh, B., Ackva, J., "Parameter-Excited Instabilities of 1- and 2-Bladed HAWTS," EWEC, Glasgow, Scotland, July 10-13, 1989.

29. Rankine, W.J.M., *Transactions, Institute of Naval Architects*, Vol. 6, p. 13, 1865.

30. Froude, R.E., *Transactions, Institute of Naval Architects*, Vol. 30, p. 390, 1889.

31. Prandtl, L., "Appendix to Scraubenpropellor mit Gerngstein Energieverlust," by Betz, A., Guttinger Nachr, 1919.

32. Goldstein, S., "On the Vortex Theory of Screw Propellers," *Proc. Royal Soc.* A123, p. 440, 1929.

33. Wilson, R.E., Walker, S.N., "Performance Analysis of HAWTS," NASA-NAG-3-278, 1984.

34. Weber, T.L., "Inclusion of Nonlinear Aerodynamics in the FLAP Code," Ninth ASME Wind Energy Symposium, New Orleans, Louisiana, January 14-18, 1990.

35. Connell, J.R., "The Spectrum of Wind Speed Fluctuations Encountered by a Rotating Blade of a WEC," PNL 4083, Pacific Northwest Laboratories, Richland, Washington, 1981.

36. Veers, P.S., "Modeling Stochastic Wind Loads on a Vertical Axis Wind Turbine," SAND83-1909, Sandia National Laboratories, 1984.

37. Walker, S.N., Weber, T.L., Wilson, R.E., "A Comparison of Wind Turbulence Simulation Models for Stochastic Loads Analysis for HAWT," SERI/STR-217-3463, June 1989.

38. Wright, A.D., Weber, T.L., Thresher, R.W., Butterfield, C.P., "Prediction of Stochastic Blade for Three-Bladed, Rigid-Hub Rotors," Ninth ASME Wind Energy Symposium, New Orleans, Louisiana, January 14-18, 1990.

39. Powles, S.J.R., Anderson, M.B., "The Effect of Stochastic and Deterministic Loading on Fatigue Damage in Large HAWT," Sir Robert McAlpine & Sons, Ltd., London, U.K., 1984.

40. Garrad, A.P., Hassan, U., "The Dynamic Response of Wind Turbines for Fatigue Life and Extreme Load Prediction," EWEC, Rome, Italy, Oct. 7-9. 1986.

41. Wilson, R.E., Hartin, J.R., "Mode Shapes for Wind Turbine Vibration Analysis," ASME J. Solar Engr., May, 1990.

42. Weber, T.L., Walker, S.N., Wilson, R.E., "Users Manual for the DRT Rotor Code," OSU, January 1991.

43. Glauret, H., "The Analysis of Experimental Results in Windmill Brake and Vortex Ring States of an Airscrew," ARC Reports and Memoranda, No. 1026, 1926.

44. Glauret, H., "On Contradiction of the Slipstream of an Airscrew," ARC Reports and Memoranda, No. 1067, 1926.

45. Kane, T.R., Levinson, D.A., *Dynamics: Theory and Applications*, McGraw-Hill Book Co, New York, 1985.

46. Musial, W.D., Butterfield, C.P., Handman, D., "ESI-80/EPRI Test Program," EPRI RP1996-14, December 1985.

47. Weber. T.L., "Turbulence Induced Loads on a Teetered Rotor," Ph.D. Thesis, 1991.

Document Control Page	1. SERI Report No. SERI/TP-257-4366	2. NTIS Accession No. DE91002190	3. Recipient's Accession No.

4. Title and Subtitle

Analysis of a Teetered, Variable-Speed Rotor - Final Report

5. Publication Date
June 1991

6.

7. Author(s)
T. L. Weber, R. E. Wilson, and S. N. Walker

8. Performing Organization Rept. No.

9. Performing Organization Name and Address

Department of Mechanical Engineering
Oregon State University
Corvallis, Oregon 97331

10. Project/Task/Work Unit No.
WE118102

11. Contract (C) or Grant (G) No.

(C) XG-0-19165-1

(G)

12. Sponsoring Organization Name and Address
Solar Energy Research Institute
1617 Cole Blvd.
Golden, CO 80401

13. Type of Report & Period Covered
Technical Report

14.

15. Supplementary Notes
SERI technical monitor: Alan Wright, (303) 231-7651

16. Abstract (Limit: 200 words)

A computer model of a horizontal axis wind turbine (HAWT) with four structural degrees of freedom has been derived and verified. The four degrees of freedom include flapwise motion of the blades, teeter motion, and variable rotor speed. Options for the variable rotor speed include synchronous, induction, and constant-tip-speed generator models with either start, stop, or normal operations. Verification is made by comparison with analytical solutions and mean and cyclic ESI-80 data. The Veers full-field turbulence model is used as a wind input for a synchronous and induction generator test case during normal operation. As a result of the comparison, it is concluded that the computer model can be used to predict accurately mean and cyclic loads with a turbulent wind input.

17. Document Analysis

a. Descriptors
horizontal wind axis turbine ; variable-speed rotor ; wind energy ; computer model

b. Identifiers/Open-Ended Terms

c. UC Categories
261

18. Availability Statement
National Technical Information Service
U.S. Department of Commerce
5285 Port Royal Road
Springfield, VA 22161

19. No. of Pages
57

20. Price
A04

Form No. 0069E (6-30-87)